10-15-2014 12:00 AM

Quantitative Analysis of Relaxation Rate Dependence on Interecho Time in MagA-expressing, Iron-labeled Cells

Casey Yesol Lee, *The University of Western Ontario*

Supervisor: Dr. Neil Gelman, *The University of Western Ontario*
Joint Supervisor: Dr. Donna Goldhawk, *The University of Western Ontario*
A thesis submitted in partial fulfillment of the requirements for the Master of Science degree in Medical Biophysics
© Casey Yesol Lee 2014

QUANTITATIVE ANALYSIS OF RELAXATION RATE DEPENDENCE ON INTERECHO
TIME IN MAGA-EXPRESSING, IRON-LABELED CELLS

(Thesis format: Integrated Article)

by

Casey Yesol <u>Lee</u>

Graduate Program in Medical Biophysics

A thesis submitted in partial fulfillment
of the requirements for the degree of
Master of Science

The School of Graduate and Postdoctoral Studies
The University of Western Ontario
London, Ontario, Canada

I

ABSTRACT

Reporter gene-based methods of labeling cells with iron is an emerging method of providing magnetic resonance imaging (MRI) contrast for long-term cell tracking and monitoring of cellular activities. This thesis investigates 9.4 T NMR properties of mammalian cells over-expressing a magnetotactic bacterial putative iron transport gene, *MagA*, and the associated untransfected parental cells. Cells were cultured in medium alone or supplemented with 250 µM ferric nitrate. Using the Carr-Purcell-Meiboom-Gill sequence, the relationship between R2 and interecho time was analyzed for each of the cell types using a model based on water diffusion in weak magnetic field inhomogeneities (Jensen and Chandra, 2000) as well as a fast-exchange model (Luz and Meiboom, 1963). Iron levels were assessed with inductively-coupled plasma mass spectrometry. As expected from previous work, the iron content in iron-supplemented, MagA-expressing cells was higher than the unsupplemented or parental cell lines. With regard to NMR, increases in R2 with increasing interecho time were typically greatest in the cells containing higher iron content. The dependence of R2 on interecho time in iron-supplemented, MagA-expressing cells was better represented by the Jensen-Chandra model compared to the Luz-Meiboom model, which is consistent with comparisons of these models in iron-containing tissues. On the other hand, the Luz-Meiboom model performed better than the Jensen-Chandra model for the remaining cell types. These findings provide insight into the high field relaxation mechanisms present in cells expressing a candidate MR reporter gene, which should be valuable for optimizing MRI contrast for long-term cell tracking and monitoring of cellular activities.

CO-AUTHORSHIP STATEMENT

Chapter 2 of this thesis has been submitted for consideration in a peer-reviewed journal (*Journal of Magnetic Resonance*). The title and authorship of this chapter follows:

Chapter 2:

Title: Investigating the Relationship between Transverse Relaxation Rate (R2) and Interecho Time in MR Reporter Gene-based Iron-labeled Cells

Authorship: CY Lee (C.Y.L.), RT Thompson (R.T.T.), FS Prato (F.S.P.), DE Goldhawk (D.E.G.), and N Gelman (N.G.)

As the primary author of this manuscript, CY Lee accomplished the following:

a) Cultured and prepared cells for the NMR experiments;

b) Performed BCA assays and prepared samples for ICP-MS analysis;

c) Acquired all NMR data;

d) Analyzed NMR data using Matlab;

e) Performed theoretical model fitting to NMR data;

f) Analyzed diffusion coefficient (D) from previously acquired MRI data;

g) Wrote the first draft of the manuscript and incorporated revisions suggested by all co-authors into the final draft.

To my parents, Sangdon Lee and Kyungsook Kim, and my sister, Tia, for their love and support

ACKNOWLEDGEMENTS

TABLE OF CONTENTS

CHAPTER 2   25

Investigating the Relationship between Transverse Relaxation Rate (R2) and Interecho Time in MRI Reporter Gene-based Iron-labeled Cells

CHAPTER 3   48

Summary and Future Work

APPENDIX   55

Curriculum Vitae

LIST OF FIGURES

LIST OF TABLES

LIST OF ABBREVIATIONS

α	angle of rotation of M away from the z-axis
Å	angstrom
γ	gyromagnetic ratio
τ	half of interecho time
2τ	interecho time
τ_c	exchange time constant (from the Luz-Meiboom model)
φ	phase
ω	precession frequency
ω_0	larmor frequency
G_0	mean-squared-magnitude of field inhomogeneity (from the Jensen-Chandra model)
K_0	mean-square-magnitude of field variations (from the Luz-Meiboom model)
r_c	spatial correlation length (from the Jensen-Chandra model)
Δx	change in x
$\frac{1}{\tau_c}$	rate of exchange (from the Luz-Meiboom model)
$\frac{1}{T_{20}}$	transverse relaxation rate in the absence of microscopic field inhomogeneities
$1 - r^2$	coefficient of non-determination
$<x>$	average over x

B	static magnetic field; $B = (B_x, B_y, B_z)$
B_{loc}	magnitude of local magnetic field
B_0	magnitude of static magnetic field B
B_1	magnitude of applied magnetic field
C	correlation function
CPMG	Carr-Purcell-Meiboom-Gill: a pulse sequence
Control cells	MagA-Fe, P+Fe, and P+Fe
D	diffusion coefficient of water
EMF	electromotive force
FDG	[^{18}F] fluoro-2-deoxy-D-glucose
Fe	Iron
FID	free induction decay
G	spatial correlation function
GFP	green fluorescent protein
Hz	Hertz
ICP-MS	inductively-coupled plasma mass spectrometry
M	macroscopic magnetization; $M = (M_x, M_y, M_z)$
M_0	magnitude of M

M_z	longitudinal component of $\boldsymbol{M}$
M_{xy}	transverse component of $\boldsymbol{M}$; $M_{xy} = \left(M_x^2 + M_y^2\right)^{1/2}$
MagA-Fe	MagA-expressing cells cultured in the absence of iron supplementation
MagA+Fe	MagA-expressing cells cultured in the presence of iron supplementation
MFI	magnetic field inhomogeneity
$MnCl_2$	Manganese Chloride
MR	magnetic resonance
MRI	magnetic resonance imaging
NMR	nuclear magnetic resonance
P	untransfected parental cell line
P-Fe	parental cells cultured in the absence of iron supplementation
P+Fe	parental cells cultured in the presence of iron supplementation
PET	positron emission tomography
r	magnitude of $\boldsymbol{r}$
$\boldsymbol{r}$	coordinate of a magnetic moment; $\boldsymbol{r}$ = (x, y, z)
R2	transverse relaxation rate
RF	radio frequency pulse
S	signal intensity
SEM	standard error of mean
SSR	sum-of-squared-residuals
SST	total sum of squares
SPIO	superparamagnetic iron oxide
t	time
T	tesla
$T_2{}^*$	effective transverse relaxation time
TE	signal echo time
x	x Cartesian coordinate
x'	x' coordinate in rotating frame of reference
y	y Cartesian coordinate
y'	y' coordinate in rotating frame of reference
z	z Cartesian coordinate

Chapter 1

INTRODUCTION

1.1 Molecular Imaging

Molecular imaging is a tool for measuring biological activities at the cellular and molecular level non-invasively [1–3]. Molecular or metabolic images offer insights for disease diagnosis and prognosis, beyond which an anatomical image may provide. This type of imaging can potentially allow earlier detection and treatment of a disease by detecting molecular abnormalities that precede anatomically visible changes. In addition, direct analysis of treatment or therapeutic outcomes may be possible by understanding the underlying molecular mechanisms of disease progression [2].

Detection of molecular activity is achieved using a probe or tracer that has a high affinity to the target molecular receptor. For example, green fluorescent protein (GFP) and luciferase-tagged antibodies [2,4] are used for optical imaging modalities such as fluorescence and bioluminescence imaging, respectively. In a clinical setting, [^{18}F] fluoro-2-deoxy-D-glucose (FDG) is widely used as a positron emission tomography (PET) tracer [1].

Each imaging modality has its own limitations. Fluorescent and bioluminescent imaging [5] provide little anatomical information due to low spatial resolution arising from high light scattering in tissues. This scattering limits the sensitivity and penetration depth of imaging, which makes whole-body clinical imaging difficult. As for PET, it requires the use of radioactive tracers; thus repeated imaging is restricted [4]. Compared to other imaging modalities such as magnetic resonance imaging (MRI), PET is also restricted with a limited spatial resolution [6]. In order to overcome these limitations, the feasibility of using MRI as a molecular imaging modality as well as the development of appropriate tracers have been actively pursued.

1.1.1 Molecular Imaging in MRI

MRI is an imaging technique, used in both research and clinical assessment, which allows non-invasive analysis on detection of anatomical and physiological processes. One advantage of MRI is that it does not require radioactive tracers as in PET [4], thus, repetitive imaging for longitudinal studies poses no risk of radiation exposure [7]. In addition, MRI provides superior soft tissue contrast with high spatial resolution [8]. For example, spatial resolutions on the order 100 μm can be achieved in small animal imaging. In order to optimize molecular imaging, contrast agents are needed to distinguish cells that are being tracked from their surrounding tissues. The possibility of molecular imaging using MRI has been actively explored in the context of cell tracking [9] to monitor therapies in areas such as tissue regeneration using cardiac and neuronal cells, and in cancer [5,10]. The contrast can be achieved through two mechanisms of cell labeling: exogenous or endogenous.

1.1.2 Exogenous Labeling

Exogenous contrast involves labeling cells with an externally introduced contrast agent such as superparamagnetic iron oxide (SPIO) particles or other metals like gadolinium (Gd) or Manganese (Mn) [8]. This labeling allows the generation of stronger contrast signals. The majority of studies suggest that there is no significant cytotoxic effect from labeling cells with iron oxide particles [4]. However, it is not clear how long metal-based contrast agents remain in non-toxic form in the body [9]. As well, previous studies [11,12] using SPIO particles discussed a potential problem associated with localizing live SPIO-labeled cells as macrophages can take up SPIO particles released by dead cells and create false signals. The cellular contrast that is generated from externally-introduced contrast agents, the magnetic resonance (MR) signal decreases with cell division and cell death [13]. Perhaps most importantly, the role of specific gene expression cannot be monitored through exogenous cell labeling as SPIO have no inherent biological activity. Thus, exogenous labeling is primarily used to indicate the location of cells and is not amenable to the study of long-term effect(s) of specific gene expression on molecular and cellular progression of a disease, as may be achieved using endogenous labeling (see Section 1.1.3).

1.1.3 Endogenous Labeling

Endogenous labeling involves generating contrast by utilizing genes overexpressed in cells. Reporter genes for MRI have been proposed as a method for tracking both cellular and molecular activities [14]. Reporter gene expression vectors consist of a regulatory promoter fused to a gene that can produce an easily detectable protein and/or contrast. Since the contrast is linked to gene expression, the signal is detected in viable cells and does not become diluted as cells divide as long as the substrate for the expressed protein is maintained [4]. In cell culture models of iron handling protein overexpression, an iron supplement may induce MR contrast [15,16]. The reporter gene method is beneficial for understanding the role of a specific gene in disease progression as well as the fate of a specific precursor cell function including migration, proliferation, and differentiation [2–4]. This method will also enable detection of cellular and molecular mechanisms that are present but difficult to detect, including proteins of interest within intracellular compartments that are not accessible to exogenous probe or contrast agent [5]. However, reporter gene expression can potentially create harmful effects. Cells transfected with a reporter gene may undergo transformations due to random integration of the newly introduced gene, raising the possibility of unwanted tumor formation, cell function or dysfunction [3]. Thus, the long-term effect of reporter gene expression on cellular function needs to be studied in greater detail.

Some examples of reporter genes, involved in intracellular iron accumulation, that have been studied as potential MR contrast agents include a modified form of mammalian ferritin [16] or *MagA*, a putative iron transporter from magnetotactic bacteria [17]. Despite lower sensitivity of reporter gene-based method to iron-label cells (e.g., providing iron contents of approximately 0.5 pg Fe/cell from *MagA* expression [18] and 0.03 pg Fe/cell from modified form of ferritin [19,20]) compared to that obtainable with SPIO particles (approximately 60 pg Fe/cell [21]), this method provides a valuable means of non-invasively studying cellular and molecular mechanisms of disease progression over the long-term, in pre-clinical models [5].

1.2 *MagA* Expression and Iron Uptake

1.2.1 Iron-based Contrast

Iron is an essential element for maintaining proper function in cells. However, free iron is toxic to cells. Therefore, the critical amount of iron needed by the body is maintained through careful regulation of iron uptake, transport, and storage. Iron homeostasis is maintained through various iron regulatory mechanisms such as the iron regulatory element, transferrin receptor, and ferritin [22].

For the purpose of producing gene-based MR contrast, several iron-handling genes have been used to iron-label cells [14]. For example, ferritin, the most abundant form of iron storage in the body, and transferrin receptor, a protein involved in iron uptake from circulating transferrin, have been studied as candidates to enhance cellular iron accumulation and improve MR contrast. Specifically, work involving both heavy-chain and light-chain subunits of ferritin have shown promise. The effectiveness of producing contrast based on various types of over-expression of modified ferritin subunits, which lack iron response elements to enable continuous expression, includes the over-expression of heavy-chain alone, light-chain alone, heavy and light chain simultaneously, heavy and light chain chimeric units, as well as the co-expression of ferritin and transferrin receptor [19,23]. In addition, researchers are actively pursuing other genes that can potentially promote greater iron accumulation and enhance MR contrast. One such prototype gene is the magnetotactic bacterial *MagA* [15].

1.2.2 *MagA*

MagA was originally thought to be involved in the formation of the magnetotactic bacterial magnetosome, a membrane enclosed compartment which contains magnetite (Fe_3O_4) [15,24,25]. While many genes are recognized today for their role in regulating magnetosome iron storage and uptake [26], *MagA* was initially characterized as an iron transport protein [27]. As a result, this gene has been exploited as a potential candidate for iron-labeling cells. Although, the exact nature and mechanism of iron biomineralization using *MagA* in mammalian cells is not clear

[14,27] and the role of *MagA* in iron storage enhancement in bacteria has been questioned [28], expression of this gene enhances the iron content in multiple mammalian cell types upon iron-supplementation [15,18,29].

Formation of magnetosome-like particles from *MagA* expression, without introducing cytotoxicity in mouse neuroblastoma (N2A) cells, has been observed with 11 T MRI [15]. Feasibility of repeated *in vivo* detection of tumor xenografts derived from MagA-expressing cells has been studied and compared to those overexpressing the modified ferritin heavy- and light-chains using 3 T MRI in a mouse model. Xenografts were examined up to 34 days post-injection based on analysis of signal voids [17]. In a clonal *MagA* cell line, Zurkiya et al. (2008) [18] showed an increase in a MR relaxation parameter (R_2) at 3 T upon iron supplementation (200 μM ferric citrate). Lastly, feasibility of using various MR relaxation parameters (denoted R_2, R_2' and R_2*) to detect iron contrast in MagA-expressing human tumor cells (MDA-MB-435) cultured in the presence of 250 μM ferric nitrate has been assessed at 3 T [29]. This study also showed that iron content in iron-supplemented MagA-expressing cells was significantly enhanced compared to non-supplemented cells. The trace elemental analysis of iron confirmed a mean value (± SEM) of 0.667 ± 0.111 μg Fe/(mg protein) in iron-supplemented, MagA-expressing cells (7 samples); whereas, only 0.047 ± 0.006 μg Fe/(mg protein) was found in non-supplemented, MagA-expressing cells (7 samples).

Based on these previous studies, *MagA* expression in mammalian cells has shown potential to enhance intracellular iron storage and consequently, iron-based MR contrast without affecting cell viability. However, to successfully utilize this MagA-based contrast effectively, a method of quantifying this iron-specific contrast is needed to improve MR cell detection.

1.3 Physics of Nuclear Magnetic Resonance (NMR)

NMR is a phenomenon that can be observed when a system of nuclei, each having a magnetic moment, is placed within a strong magnetic field. This phenomenon has been exploited by chemists, biochemists, and physicists to investigate the chemical and physical environments of protons or other magnetic nuclei within particular materials or tissues. Combining NMR with methods of spatial encoding leads to magnetic resonance imaging (MRI), a tool that can provide images of the macroscopic structure of biological systems. Since NMR experiments are less time-consuming and often provide more ideal experimental conditions (e.g., more uniform magnetic fields) than MRI, it is sometimes worthwhile to utilize NMR to explore biological materials/tissues before attempting translation to MRI (*in-vitro* and *in-vivo*). This thesis reports the results of NMR experiments performed on cells that have been transfected with a reporter gene (*MagA*) and their parental controls. The following sections provide background on NMR and more specifically, on the NMR measures utilized in this thesis.

1.3.1 Background on NMR

In the absence of an external magnetic field proton magnetic moments are randomly oriented. In order to observe a proton NMR signal, a sample of interest is placed in a strong static magnetic field (B_0). Each proton magnetic moment in the sample tends to align either parallel or anti-parallel to the direction of the main magnetic field (z-axis). The proton magnetization (M), which will be simply referred to as the 'magnetization' from here onward, is the vector sum of individual proton magnetic moments. At thermal equilibrium, M is static along the z-axis as more magnetic moments are aligned parallel to the z-axis (more favourable state) than that are anti-parallel. The magnitude of M at thermal equilibrium is referred to as M_0. When M is rotated away from the z-axis, it precesses about the z-axis with a frequency known as the larmor frequency (ω_0), defined by:

$$\omega_0 = \gamma B_0 , \qquad (1.1)$$

where γ denotes the gyromagnetic ratio. For the proton, $\gamma/(2\pi)$ is equal to 42.6 MHz/T.
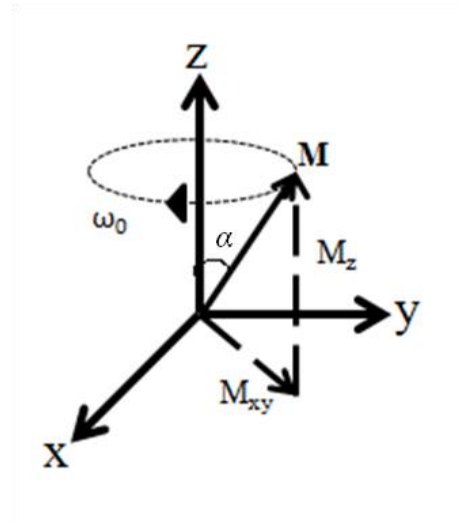
Figure 1.1 Components of a net magnetization vector (**M**): M_{xy} and M_z.

Consider a 'rotating frame of reference' (with a coordinate system: x′, y′, and z) that is precessing at ω_0 about the z-axis with respect to the laboratory frame. In order to generate an NMR signal, a second magnetic field (B_1), that is circularly polarized and has a frequency close to ω_0, is applied along either the x′- or y′-axis. While B_1 is applied, **M** effectively rotates about B_1 with a frequency equal to γB_1, i.e., it rotates away from the z-axis towards the x-y plane. Therefore, the angle of rotation (α) of **M** is dependent on the duration and amplitude of B_1. This transient B_1 magnetic field is known as a radio frequency (RF) pulse. Once **M** is no longer parallel to the direction of B_0, it precesses about the z-axis with angular frequency ω_0. Precession of the transverse component of **M** (M_{xy}) induces an electromotive force (EMF) in the receiver coil, which is recorded by a digital voltmeter and called the NMR signal.

1.3.2 Free Induction Decay

The free induction decay (FID) refers to the MR signal decay following a 90° RF pulse and is associated with the decay of the net transverse magnetization within the NMR sample. The evolution of this net transverse magnetization can be understood by recognizing that the magnetic field experienced by the protons often varies spatially. Using notation similar to that previously used by Jensen and Chandra (2000), we can express this mathematically as,

$$B(r(t)) = B_0 + B_{loc}(r(t)) , \qquad\qquad (1.2)$$

where B is the actual magnetic field experienced by protons, B_{loc} is a local magnetic field contribution which accounts for spatial variation of the total magnetic field, $r(t)$ represents the coordinate of a proton magnetic moment that changes with time, t. (The time dependence has been included here as it will be helpful later on.) The local magnetic field is several orders of magnitude smaller than B_0 and varies over distance scales from microscopic to macroscopic. For example, the local magnetic fields produced by iron particles typically vary over microscopic distance scales. Therefore, the actual magnetic field strength $B(r)$ experienced by the magnetic moments in a given region is dependent on $B_{loc}(r(t))$, which relies on both the location of protons in the inhomogeneous magnetic field as well as the change in B_{loc} protons experience as they diffuse through microscopic magnetic field inhomogeneities (MFI).

In a classical description, a magnetic moment at a given location precesses with a frequency $\omega(r(t)) = \gamma B(r(t))$. According to this relationship between ω and B, magnetic moments residing in locations with different local magnetic fields precess with different frequencies. This leads to a spatial distribution of phase ($\varphi(r(t)) = -\int_0^t \omega(r(t')) \, dt'$), with respect to the phase of a magnetic moment that experiences the static frequency, ω_0.
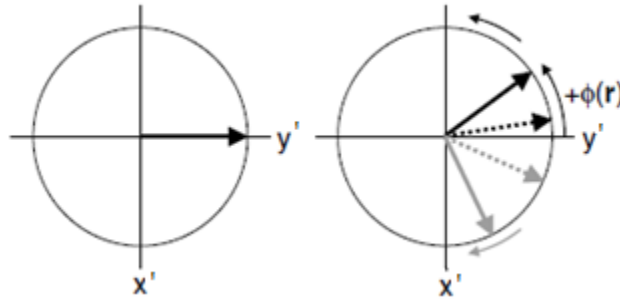
Figure 1.2[a] Dephasing of magnetic moments. Magnetic moments begin to lose phase coherence as individual moments acquire distinct phase.
[a] Figure source: Fig. 1.22 (B,C) from 'In vivo NMR spectroscopy'[30]

In the rotating frame, the initial net magnetization following the 90° RF pulse appears to be stationary as the reference frame is also precessing at ω_0 in the laboratory frame. However, as the spatial variation of phase accumulates, the vector sum of magnetic moments gradually decreases to zero. This loss of the initial phase coherence of M following the RF pulse is called de-phasing.

The degree of de-phasing accumulates over time, leading to the net transverse magnetization decay.

An additional source of transverse magnetization decay is provided by proton-proton dipolar interactions. In some sense, this can also be thought of as a form of de-phasing due to magnetic fields of neighboring proton magnetic moments. However, because of its different behaviour, particularly in the spin-echo to be described below, one might think of this qualitatively as producing a "shortening" (rather than de-phasing) of the magnetization within regions (often called isochromats) that are small compared to the distance over which $B_{loc}(r(t))$ varies. The combined effect of this shortening and de-phasing lead to decay of the net transverse magnetization and hence, the FID, which is often approximately exponential in form, such as

$$S(t) = S(0)e^{-t \cdot R_2^*}, \quad (1.3)$$

where R_2^* indicates the effective transverse relaxation rate and S indicates signal as a function of t.

1.3.3 Echoes

The initial de-phasing of magnetic moments can be 'reversed' by application of a 180° RF pulse about the x'- or y'-axis. In Fig. 1.3, the 180° RF pulse is applied along the y'-axis.
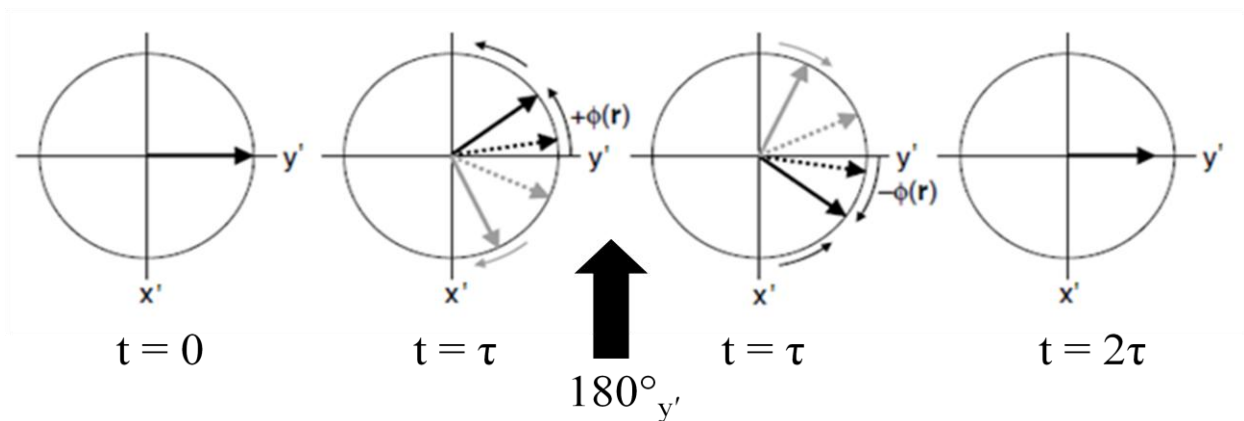
Figure 1.3[a] Spin echo formation. The initial de-phasing of magnetic moments is reversed by the application of a 180° RF pulse along the y'-axis.
[a] Figure source: Fig. 1.22 (B − E) from 'In vivo NMR spectroscopy'[30]

This pulse does not change the $\omega(r(t))$ of a magnetic moment at a given location but reverses its already accumulated phase angle. Suppose the changes in $r(t)$ experienced by magnetic moments are small (i.e., water movement is restricted), then the application of the 180° RF pulse at time τ following the initial 90° RF pulse will reverse the de-phasing of magnetic moments, leading to the formation of a 'spin echo' at time 2τ. In such case, the decrease in the magnitude of spin echo, or signal, is just due to the proton-proton dipolar interactions, which are irreversible. The signal as a function of 2τ commonly decays in exponential form such as,

$$S_{2\tau} = S(0)e^{-2\tau \cdot R_2}, \quad (1.4)$$

from which the time-varying transverse relaxation rate, R_2, can be determined by acquiring several signals with different τ values. (If multiple signal averages that are acquired with the repetition time $(TR) \ll T_1$, where T_1 indicates the longitudinal relaxation time, the overall signal amplitude will also depend on T_1. However, this will not affect the R_2 measurements as long as $TR - TE$ is kept constant for all acquisitions.) The total transverse relaxation (R_2^*, eq. 1.3) includes this irreversible rate (R_2) as well as a reversible component known as R_2', i.e., $R_2^* = R_2 + R_2'$.

However, if $B_{loc}(r(t))$ changes during this period (e.g., due to diffusion of magnetic moments through MFI produced by the presence of iron particles), the reversal of de-phasing of magnetic moments becomes incomplete. Consequently, the magnitude of the spin echo will be lower compared to that formed in the absence or lesser degree of $B_{loc}(r(t))$ change.

1.3.4 The Carr-Purcell-Meiboom-Gill Sequence

The Carr-Purcell-Meiboom-Gill (CPMG) sequence [31,32] applies a series of refocusing pulses (ideally 180°) separated by the interecho time (2τ) after initially perturbing M from its thermal equilibrium with a 90° pulse. As shown in Fig. 1.4, this sequence forms multiple echoes that are separated by 2τ. The value of R_2, as a function of 2τ, can be determined from studying the decay in the strength of these multiple echoes, often in the exponential form such as,

$$S_n = S(0)e^{-2\tau n \cdot R_2}, \quad (1.5)$$

where n indicates the nth echo.

In order to minimize the error in R_2 measurement arising from imperfect refocusing pulses, these pulses are phase-shifted by 90° in the transverse plane relative to that of the initial excitation pulse, implying that if an excitation pulse was applied along the x′-axis, then the refocusing RF pulses will be applied along the y′-axis. The RF pulses are applied in even numbers to further reduce the errors associated with imperfect refocusing pulses. Imperfect 180° RF pulses will lead to incomplete transfer of magnetization onto the x′-y′ plane. This remaining z-magnetization will be refocused at a later time leading to unwanted contributions to the echo signals. As large numbers of RF pulses are applied in the CPMG sequence, errors rising from each imperfect RF pulse will accumulate and results in inaccurate R_2 measurement.
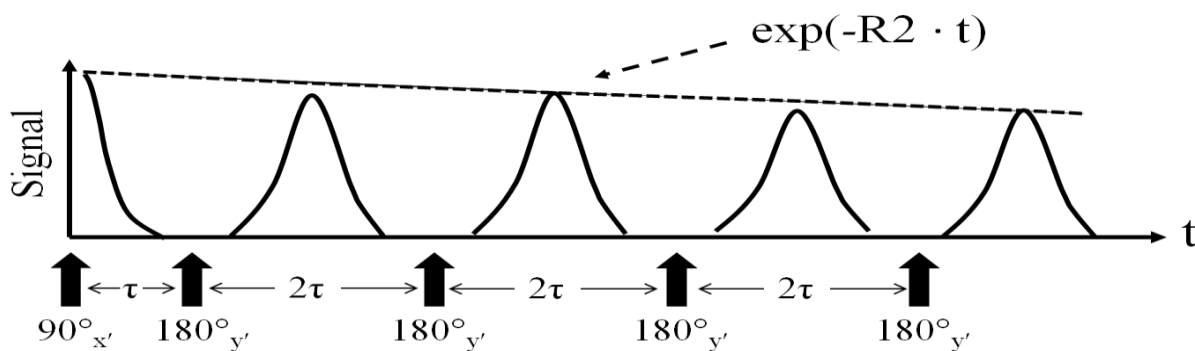
Figure 1.4 The CPMG sequence. The echoes are formed as 180° RF pulses reverse the de-phased magnetic moments.

For the work presented in this thesis, each signal echo in the CPMG sequence was acquired separately using the sequence provided by the vendor. The single echo acquisition method is different from a more standard CPMG measurement that acquires full series of multiple echoes, for a given 2τ value, i.e., the echo signal following each refocusing pulse is acquired. This single echo acquisition method requires a longer time to acquire a full-series of echoes as only the last echo (or decay of the last echo) of the series is acquired. The longer acquisition time is advantageous for chemical analysis as it provides higher spectral resolution for viewing multiple spectral peaks.

In the single echo acquisition method, a train of RF pulses is applied such that the time from the initial 90° pulse to the final echo signal is equal to the desired echo time (TE). The value of TE is then equal to the number of RF pulses times 2τ. Multiple values of TE, required to create the R_2 decay curve, are then obtained by adjusting the number of RF pulses for each of a set of acquisitions. The value of R_2, for a given 2τ, is then calculated using the individually acquired multiple echo signals and eqn. 1.5.

1.4 R_2 Dependence on 2τ

The R_2 dependence on 2τ emerges as the change in $B_{loc}(\boldsymbol{r}(t))$ experienced by protons of water molecules change as the de-phasing period (duration of 2τ) varies in the CPMG sequence. When 2τ is short, diffusing protons on average experience only small change in B_{loc} and hence, the de-phasing is largely reversible. As 2τ increases, so does the change in B_{loc} experienced by protons over the de-phasing period, which leads to less reversible signal decay and hence, increased R_2.

The sources of variation in B_{loc} experienced by protons, and hence MFI, depend on the biological settings (e.g., distribution and/or form of iron particles) of a given system. In order for water molecules to experience the change in B_{loc}, they would have to be moving through these spatially-varying MFI. The average displacement of water molecules during the de-phasing period depends on factors such as water diffusion rate, ability to cross the cellular membrane, and/or interaction with protein (hence, impeding the water movement).

Experimentally, several studies have found that R_2 increases with 2τ in biological samples, especially in iron-containing tissues [33–41]. A summary of R_2 dependence on 2τ found in various reports are provided in Table 1.1.

Table 1.1. Summary of R_2 dependence on 2τ from the previous reports

Reported by	Sample	B_0 (T)	Note
Vymazal *et al*. (1996) [42]	Brain (frontal cortex, caudate nucleus, putamen, and globus pallidus)	1.5	R_2 ranging between ~ 14 – 18 s^{-1} (GP), 11 – 13 s^{-1} (PUT, CN), and 9 – 10 s^{-1} (FC)
Ye *et al*. (1996) [36]	Brain (globus pallidus, putamen, caudate nucleus, and thalamus)	2.35	R_2 ranging between ~ 19 – 26 s^{-1} (GP), 16 – 19 s^{-1} (PUT), 14 – 16 s^{-1} (TH), and 11 – 13 s^{-1} (CN)
Brooks *et al*. (1995) [43]	Deoxygenated blood; Globus Pallidus	1	R_2 ranging between ~ 10 – 35 s^{-1} (blood) and 13.5 – 16.5 s^{-1} (GP)
Hocq *et al*. (2009) [35]	Brain (caudate nucleus, globus pallidus, putamen, substantia nigra); Liver; Spleen	4, 7	R_2 ranging between 100 – 140 s^{-1} (Spleen, 7T), 120 – 160 s^{-1} (Liver, 7T)
Vymazal *et al*. (1996) [42]	White matter	1.5	Minimal R_2 dependence on 2τ
Brooks *et al*. (1995) [43]	Oxygenated blood	1	Minimal R_2 dependence on 2τ compared to deoxygenated blood

Based on these findings, the dominant R_2 dependence on 2τ in many tissues appears to be an iron-dependent effect. This is supported by the observation that this dependence is weaker in low iron tissues samples (i.e., white matter [42] or oxygenated blood [43]) compared to tissues with higher iron contents (i.e., liver, spleen, globus pallidus). In fact, Ye *et al*. [36] found that the dependence of R_2 on 2τ increases as tissue iron concentration increases in brain tissues samples, adding further supports to this claim. In addition, previous studies have found a linear relationship between R_2 and B_0 in ferritin [44], in tissue regions (*in vivo*), and in tissue samples (*in vitro*) [34,35,43]. Therefore, it is expected that dependence of R_2 on 2τ would increase with field strength.

There have been attempts to quantitatively assess the microscopic parameters that may be responsible for the R_2 dependence on 2τ. Amongst previously proposed models to describe this relationship between R_2 and 2τ [45–48], my thesis work utilizes the two specific models developed by 1. Luz and Meiboom and 2. Jensen and Chandra. The model by Luz and Meiboom [49] was developed based on the effect of fast-exchange of water between 'distinct' compartments and is described in detail in section 1.4.1. The other proposed model (Jensen and Chandra [50]) was developed for a system with continuous water diffusion through MFI (see section 1.4.2). These two models have been previously applied to iron-containing tissues or blood samples that have been found to exhibit an observable R_2 dependence on 2τ. However, my thesis is the first report to describe and apply these theoretical models [49,50] to the R_2 dependence on 2τ in gene-based, iron-labeled cells.

1.4.1 The Luz-Meiboom (Fast Exchange) Model

The Luz-Meiboom model [49] was introduced by Luz and Meiboom in 1963 to study an experimental system where chemical exchange of water between two well-defined sites was known to be the major source of local magnetic field variation. Although applied to describe experimental observations from this two site, chemical exchange system, the theoretical model is more general in nature (refer to the appendix of Luz and Meiboom (1963)). This model assumes that there are 'distinct' environments/compartments and that a fast-exchange of water molecules is occurring between those environments, allowing water molecules to experience the change in

B_{loc} as they move from one environment to another. Under these assumptions, Luz and Meiboom derived an equation to describe the relationship between R_2 and 2τ. This model, in a form described by Jensen and Chandra (2000) [50], is written as,

$$R_2 = \gamma^2 K_0 \tau_c \left[1 - \frac{\tau_c}{\tau} \tanh \frac{\tau}{\tau_c}\right] + \frac{1}{T_{20}} , \qquad (1.6)$$

where K_0 represents is the variance of the microscopically inhomogeneous magnetic field, $\frac{1}{\tau_c}$ indicates the rate of exchange, and $\frac{1}{T_{20}}$ is the transverse relaxation rate in the absence of exchange [50].

Originally, this model did not assume that there is a restriction on the number of compartments in which protons can undergo an exchange, but does assume a common lifetime (τ_c) for each compartment. However, in previous reports [35,39,43,51] using this model for experimental studies of blood and brain tissues, the Luz-Meiboom model is often conceptually described as having just two compartments (i.e., red blood cells and plasma of blood).

1.4.2 The Jensen-Chandra (Diffusion-based) Model

In 2000, Jensen and Chandra derived an equation [50] to describe the dependence of R_2 on 2τ in iron-containing systems based on the effect of water diffusion through MFI. This model was developed using the concept of an autocorrelation function, which describes the correlation between values of parameter, which is a function of time or space, and values of the same parameter but displaced in time or space.

The parameters of the Jensen-Chandra model relate to the spatial correlation function of the local magnetic field. For a simple one-dimensional system, for example, a correlation function (C) in terms of B_{loc} can be described by,

$$C(\Delta x) = \langle B_{loc}(x) B_{loc}(x + \Delta x) \rangle , \qquad (1.7)$$

where x refers to a distinct point in space, Δx is the change in x, and angle brackets ($< >$) represent the average over x. Following this, $C(0)$ is B_{loc}^2 averaged over all space (x).

Jensen and Chandra (2000) assumed that B_{loc} is a random function of space with zero mean value (i.e., $<B_{loc}(x)> = 0$). In one-dimensional terms, the correlation function $C(\Delta x)$ is defined as the product of $B_{loc}(x)$ and $B_{loc}(x+\Delta x)$ averaged over x. For a small Δx, there is a higher probability that the values of $B_{loc}(x)$ and $B_{loc}(x+\Delta x)$ are more strongly correlated (leading to the higher C). On the contrary, with increasing Δx, the variation in $B_{loc}(x)$ is more likely to increase over the interval of Δx, consequently providing lower C values. Therefore, the value of C decreases as a function of Δx. In the Jensen-Chandra model, the three-dimensional angle-averaged spatial correlation function (G) is approximated as a Gaussian distribution characterized by the spatial correlation length (r_c),

$$G(r) \approx G_0 e^{-\left(r/r_c\right)^2}, \quad (1.8)$$

where $r = |\boldsymbol{r}|$. (The parameter r replaces the term Δx in Eqn. 1.7 for the three-dimensional system.) Based on these assumptions, Jensen and Chandra derived an equation to describe the relationship between R_2 and 2τ,

$$R_2 = \left(\frac{G_0 \gamma^2 r_c^2}{2D}\right) F\left(\frac{4D\tau}{r_c^2}\right) + \frac{1}{T_{20}}, \qquad (1.9)$$

where G_0 is the variance of the microscopically inhomogeneous magnetic field, r_c denotes the spatial correlation length associated with the microscopic magnetic field inhomogeneity, D refers to the diffusion coefficient of water within the cells or tissues, and $\frac{1}{T_{20}}$ is the transverse relaxation rate in the absence of these microscopic field inhomogeneities. The function F is defined by [50],

$$F(x) = \frac{1}{\sqrt{\pi}} \int_0^\infty dy \frac{e^{-y}}{\sqrt{y}} \left[1 - \frac{1}{xy} \tanh xy\right]. \qquad (1.10)$$

This model was developed based on the effect of water diffusion (hence, 'diffusion-based') in a weakly magnetic, inhomogeneous field. Therefore, this model may be a more accurate representation of the relationship between R_2 and 2τ, in iron-containing cells or tissues, than the Luz-Meiboom model, which assumes that there are 'distinct' compartments between which water undergoes exchange (refer to Section 1.4.1). So far, this model has been applied to iron-containing systems such as blood, liver, or brain tissues [50–53].

1.4.3 Comparing the Luz-Meiboom and the Jensen-Chandra Models

The applicability of the two models, the Luz-Meiboom and the Jensen-Chandra models, have been experimentally tested and compared in blood, brain, and liver tissues [50–52]. Two of these studies [51,52] compared the performance of the two models on experimentally acquired R_2 versus 2τ data measured from human blood at 2.35, 3, and 7 T. This comparison was based on the sum-of-squared-residuals (*SSR*). In these cases, the Jensen-Chandra model provided an *SSR* that was lower (by approximately 30% or more) than that obtained with the Luz-Meiboom model. Such comparisons were also performed [50] using R_2 versus 2τ experimental data (that had been obtained in studies prior to ref. [50]) from brain regions (globus pallidus, putamen, thalamus, caudate nucleus) [36], rat liver [38], and red blood cell suspensions [39,43]. The Jensen-Chandra model provided lower *SSR* values (by over 50%) than the Luz-Meiboom model for high iron regions in brain (globus pallidus and putamen), blood, and liver. However, for the low iron regions (thalamus and caudate nucleus), the difference in *SSR* was much smaller and the fits were comparable.

The comparisons done so far suggest that the Jensen-Chandra model may provide a more accurate fitting than the Luz-Meiboom model for blood, liver, and brain regions with high iron content. In order to validate that this is true for other biological settings, further studies comparing the two models are needed. In general, greater analyses of both models and their implication(s) would be valuable in different systems as the applicability of these models may depend on the particular experimental system investigated. Toward this objective, the present thesis examines the case of gene-based, iron-labeled cells, in which the model applications are yet to be investigated.

1.5 Thesis Overview

1.5.1 Thesis Objective

There have been attempts to characterize and improve iron-based MR contrast in gene-based, iron-labeled cells in the past [14]. However, further work is needed to improve both the contrast and detection methods, as commonly used techniques are influenced by non-iron specific measures. An ideal strategy would be to identify iron-specific MRI measures that have reduced contributions from iron-independent sources. Performing NMR experiments on these gene-based iron-labeled cells provides a method to study the MR properties of these cells under experimental conditions that are more ideal (e.g., more uniform magnetic fields) than provided by MRI. Information gained from NMR can then aide in translation to MRI by helping to determine hardware and software requirements needed to perform measurements with MRI.

This thesis discusses NMR studies performed on iron-supplemented and -unsupplemented MagA-expressing mammalian cells and their parental controls. (As indicated in section 1.2.2. *MagA* expression in mammalian cells has been shown to provide a means to iron-label cells for MRI-based cell tracking [14].) The influence of *MagA* expression and iron supplementation on the R_2-enhancement with the increasing interecho time (2τ) measured with the CPMG sequence is reported in this thesis. To the best of my knowledge, this is the first work experimentally investigating and describing the relationship between R_2 and 2τ in gene-based iron-labeled cells.

The specific objectives of this thesis are:

1. To assess whether there is a relationship between R_2 and 2τ in iron-supplemented, MagA-expressing cells, similar to that observed in iron-containing tissues and different from untransfected control cells.
2. To apply and compare theoretical models based on the effects of proton exchange (the Luz-Meiboom model) or water-diffusion (the Jensen-Chandra model) to the experimentally determined relationship between R2 and 2τ in these cells.

1.5.2 Thesis Outline

The objectives of this thesis are addressed in Chapter 2, which has been submitted to *Journal of Magnetic Resonance* and the co-authorship is provided on page III. Chapter 2 presents the measurement of R_2 as a function of 2τ in iron- and non-supplemented, MagA-expressing cells and the associated parental cell line. The performance of the Luz-Meiboom and the Jensen-Chandra models were compared in terms of their efficacy to describe these relationships. Iron measurements were acquired from these cell samples and were used to help in the interpretation of the results. Chapter 3 provides a summary and discussion of the findings in this thesis. Lastly, Appendix I contains my curriculum vitae.

1.6 References

[1]   J.M. Hoffman, S.S. Gambhir, Molecular imaging: the vision and opportunity for radiology in the future., Radiology. 244 (2007) 39–47. doi:10.1148/radiol.2441060773.

[2]   T.F. Massoud, S.S. Gambhir, Molecular imaging in living subjects: seeing fundamental biological processes in a new light., Genes Dev. 17 (2003) 545–80. doi:10.1101/gad.1047403.

[3]   H. Youn, J.-K. Chung, Reporter gene imaging., AJR. Am. J. Roentgenol. 201 (2013) W206–14. doi:10.2214/AJR.13.10555.

[4]   M. Srinivas, I. Melero, E. Kaempgen, C.G. Figdor, I.J.M. de Vries, Cell tracking using multimodal imaging., Contrast Media Mol. Imaging. 8 (2013) 432–8. doi:10.1002/cmmi.1561.

[5]   M.H. Vandsburger, M. Radoul, B. Cohen, M. Neeman, MRI reporter genes: applications for imaging of cell survival, proliferation, migration and differentiation., NMR Biomed. 26 (2013) 872–84. doi:10.1002/nbm.2869.

[6]   M.F. Kircher, S.S. Gambhir, J. Grimm, Noninvasive cell-tracking methods., Nat. Rev. Clin. Oncol. 8 (2011) 677–88. doi:10.1038/nrclinonc.2011.141.

[7]   F.S. Prato, A. Thomas, A. Legros, J. Robertson, J. Mondolo, R. Stodilka, et al., MRI safety not scientifically proven, Science (80-.). 328 (2010) 568–569.

[8]   D. McRobbie, E. Moore, M. Graves, M. Prince, MRI From Picture to Proton, 2nd ed., Cambridge University Press, Cambridge, UK, 2007.

[9]   J.W.M. Bulte, I.D. Duncan, J.A. Frank, In Vivo Magnetic Resonance Tracking of Magnetically Labeled Cells After Transplantation TRANSPLANTABLE NEURAL PRECURSORS, (2002) 899–907.

[10]   M. Vandsburger, Cardiac Cell Tracking with MRI Reporter Genes: Welcoming a New Field., Curr. Cardiovasc. Imaging Rep. 7 (2014) 9250. doi:10.1007/s12410-013-9250-0.

[11]   J. Terrovitis, M. Stuber, A. Youssef, S. Preece, M. Leppo, E. Kizana, et al., Magnetic resonance imaging overestimates ferumoxide-labeled stem cell survival after transplantation in the heart., Circulation. 117 (2008) 1555–62. doi:10.1161/CIRCULATIONAHA.107.732073.

[12]   Y. Amsalem, Y. Mardor, M.S. Feinberg, N. Landa, L. Miller, D. Daniels, et al., Iron-oxide labeling and outcome of transplanted mesenchymal stem cells in the infarcted myocardium., Circulation. 116 (2007) I38–45. doi:10.1161/CIRCULATIONAHA.106.680231.

[13]   A.S. Arbab, L.A. Bashaw, B.R. Miller, E.K. Jordan, B.K. Lewis, H. Kalish, et al.,
       Radiology Characterization of Biophysical and Metabolic Properties of Cells Labeled with
       Superparamagnetic Iron Oxide Nanoparticles and Transfection Agent for Cellular MR
       Imaging 1, (2003).

[14]   D.E. Goldhawk, R. Rohani, A. Sengupta, N. Gelman, F.S. Prato, Using the magnetosome
       to model effective gene-based contrast for magnetic resonance imaging., Wiley Interdiscip.
       Rev. Nanomed. Nanobiotechnol. 4 (2012) 378–88. doi:10.1002/wnan.1165.

[15]   D.E. Goldhawk, C. Lemaire, C.R. Mccreary, R. Mcgirr, S. Dhanvantari, R.T. Thompson,
       et al., Magnetic Resonance Imaging of Cells Overexpressing MagA , an Endogenous
       Contrast Agent for Live Cell Imaging, Mol. Imaging. 8 (2009) 129–139.
       doi:10.2310/7290.2009.00006.

[16]   G. Genove, U. DeMarco, H. Xu, W.F. Goins, E.T. Ahrens, A new transgene reporter for
       in vivo magnetic resonance imaging., Nat. Med. 11 (2005) 450–4. doi:10.1038/nm1208.

[17]   R. Rohani, R. Figueredo, Y. Bureau, J. Koropatnick, P. Foster, R.T. Thompson, et al.,
       Imaging Tumor Growth Non-invasively Using Expression of MagA or Modified Ferritin
       Subunits to Augment Intracellular Contrast for Repetitive MRI., Mol. Imaging Biol. 16
       (2014) 63–73. doi:10.1007/s11307-013-0661-8.

[18]   O. Zurkiya, A.W.S. Chan, X. Hu, MagA is sufficient for producing magnetic
       nanoparticles in mammalian cells, making it an MRI reporter., Magn. Reson. Med. 59
       (2008) 1225–31. doi:10.1002/mrm.21606.

[19]   A.E. Deans, Y.Z. Wadghiri, L.M. Bernas, X. Yu, B.K. Rutt, D.H. Turnbull, Cellular MRI
       contrast via coexpression of transferrin receptor and ferritin., Magn. Reson. Med. 56
       (2006) 51–9. doi:10.1002/mrm.20914.

[20]   Y. Feng, Q. Liu, J. Zhu, F. Xie, L. Li, Efficiency of ferritin as an MRI reporter gene in
       NPC cells is enhanced by iron supplementation., J. Biomed. Biotechnol. 2012 (2012)
       434878. doi:10.1155/2012/434878.

[21]   C. Heyn, J. a Ronald, L.T. Mackenzie, I.C. MacDonald, A.F. Chambers, B.K. Rutt, et al.,
       In vivo magnetic resonance imaging of single cells in mouse brain with optical validation.,
       Magn. Reson. Med. 55 (2006) 23–9. doi:10.1002/mrm.20747.

[22]   N.C. Andrews, P.J. Schmidt, Iron homeostasis., Annu. Rev. Physiol. 69 (2007) 69–85.
       doi:10.1146/annurev.physiol.69.031905.164337.

[23]   B. Iordanova, E.T. Ahrens, In vivo magnetic resonance imaging of ferritin-based reporter
       visualizes native neuroblast migration., Neuroimage. 59 (2012) 1004–12.
       doi:10.1016/j.neuroimage.2011.08.068.

[24]   D. Schüler, Genetics and cell biology of magnetosome formation in magnetotactic bacteria., FEMS Microbiol. Rev. 32 (2008) 654–72. doi:10.1111/j.1574-6976.2008.00116.x.

[25]   A. Arakaki, H. Nakazawa, M. Nemoto, T. Mori, T. Matsunaga, Formation of magnetite by bacteria and its application., J. R. Soc. Interface. 5 (2008) 977–99. doi:10.1098/rsif.2008.0170.

[26]   I. Kolinko, A. Lohße, S. Borg, O. Raschdorf, C. Jogler, Q. Tu, et al., Biosynthesis of magnetic nanostructures in a foreign organism by transfer of bacterial magnetosome gene clusters., Nat. Nanotechnol. 9 (2014) 193–7. doi:10.1038/nnano.2014.13.

[27]   C. Nakamura, J.G. Burgess, K. Sode, T. Matsunaga, An Iron-regulated Gene, magA, Encoding an Iron Transport Protein of Magnetospirillum sp. Strain AMB-1, J. Biol. Chem. 270 (1995) 28392–28396. doi:10.1074/jbc.270.47.28392.

[28]   R. Uebe, V. Henn, D. Schüler, The MagA protein of Magnetospirilla is not involved in bacterial magnetite biomineralization., J. Bacteriol. 194 (2012) 1018–23. doi:10.1128/JB.06356-11.

[29]   A. Sengupta, K. Quiaoit, R.T. Thompson, F.S. Prato, N. Gelman, D.E. Goldhawk, Biophysical features of MagA expression in mammalian cells: implications for MRI contrast., Front. Microbiol. 5 (2014) 1–9. doi:10.3389/fmicb.2014.00029.

[30]   R.A. De Graaf, In Vivo NMR Spectroscopy - Principles and Techniques, 2nd ed., John Wiley & Sons, Ltd, West Sussex, England, 2007.

[31]   H.Y. Carr, E.M. Purcell, Effects of Diffusion on Free Precession in Nuclear Magnetic Resonance Experiments, Phys. Rev. 94 (1954) 630–638.

[32]   S. Meiboom, D. Gill, Modified Spin-Echo Method for Measuring Nuclear Relaxation Times, Rev. Sci. Instrum. 29 (1958) 688. doi:10.1063/1.1716296.

[33]   K.R. Thulborn, J.C. Waterton, P.M. Matthews, G.K. Radda, Oxygenation dependence of the transverse relaxation time of water protons in whole blood at high field, Biochim. Biophys. Acta. 714 (1982) 265–270.

[34]   J. Vymazal, R. a Brooks, N. Patronas, M. Hajek, J.W. Bulte, G. Di Chiro, Magnetic resonance imaging of brain iron in health and disease., J. Neurol. Sci. 134 Suppl (1995) 19–26. http://www.ncbi.nlm.nih.gov/pubmed/8847541.

[35]   A. Hocq, N. Brouette, S. Saussez, M. Luhmer, P. Gillis, Y. Gossuin, Variable-field relaxometry of iron-containing human tissues: a preliminary study., Contrast Media Mol. Imaging. 4 (2009) 157–64. doi:10.1002/cmmi.275.

[36] F.Q. Ye, W.R. Wayne Martin, P.S. Allen, Estimation of the iron concentration in excised gray matter by means of proton relaxation measurements., Magn. Reson. Med. 35 (1996) 285–9. http://www.ncbi.nlm.nih.gov/pubmed/8699938.

[37] B. Stefanovic, J.G. Sled, G.B. Pike, Quantitative T2 in the occipital lobe: the role of the CPMG refocusing rate., J. Magn. Reson. Imaging. 18 (2003) 302–9. doi:10.1002/jmri.10360.

[38] Y. Rozenman, X. Zou, H. Kantor, Signal loss induced by superparamagnetic iron oxide particles in NMR spin-echo images: the role of diffusion., Magn. Reson. Med. 14 (1990) 31–39. http://www.ncbi.nlm.nih.gov/pubmed/2352471.

[39] F.Q. Ye, P.S. Allen, Relaxation enhancement of the transverse magnetization of water protons in paramagnetic suspensions of red blood cells., Magn. Reson. Med. 34 (1995) 713–20. http://www.ncbi.nlm.nih.gov/pubmed/8544692.

[40] J.M. Gomori, R.I. Grossman, H.R. Drott, MR relaxation times and iron content of thalassemic spleens: an in vitro study., AJR. Am. J. Roentgenol. 150 (1988) 567–9. doi:10.2214/ajr.150.3.567.

[41] R.G. Bryant, K. Marill, C. Blackmore, C. Francis, Magnetic relaxation in blood and blood clots., Magn. Reson. Med. 13 (1990) 133–44. http://www.ncbi.nlm.nih.gov/pubmed/2319929.

[42] J. Vymazal, R.A. Brooks, C. Baumgarner, V. Tran, D. Katz, J.W.M. Bulte, et al., The relation between brain iron and NMR relaxation times: an in vitro study, Magn. Reson. Med. 35 (1996) 56–61.

[43] R.A. Brooks, J. Vymazal, J.W. Bulte, C.D. Baumgarner, V. Tran, Comparison of T2 Relaxation in Blood, Brain, and Ferritin, J. Magn. Reson. Imaging. 5 (1995) 446–450.

[44] J. Vymazal, R. a Brooks, O. Zak, C. McRill, C. Shen, G. Di Chiro, T1 and T2 of ferritin at different field strengths: effect on MRI., Magn. Reson. Med. 27 (1992) 368–74. http://www.ncbi.nlm.nih.gov/pubmed/1334206.

[45] K. Keating, R. Knight, A laboratory study to determine the effect of iron oxides on proton NMR measurements, Geophysics. 72 (2007) E27–E32. doi:10.1190/1.2399445.

[46] R. a Brooks, F. Moiny, P. Gillis, On T2-shortening by weakly magnetized particles: the chemical exchange model., Magn. Reson. Med. 45 (2001) 1014–20. http://www.ncbi.nlm.nih.gov/pubmed/11378879.

[47] C.H. Ziener, T. Kampf, P.M. Jakob, W.R. Bauer, Diffusion effects on the CPMG relaxation rate in a dipolar field., J. Magn. Reson. 202 (2010) 38–42. doi:10.1016/j.jmr.2009.09.016.

[48]   J.P. Carver, M. Biophysics, A General Two-Site Solution for the Chemical Exchange
       Produced Dependence of T2 Upon the Carr-Purcell Pulse Separation, J. Magn. Reson. 105
       (1972) 89–105.

[49]   Z. Luz, S. Meiboom, Nuclear Magnetic Resonance Study of the Protolysis of
       Trimethylammonium Ion in Aqueous Solution—Order of the Reaction with Respect to
       Solvent, J. Chem. Phys. 39 (1963) 366–370. doi:10.1063/1.1734254.

[50]   J.H. Jensen, R. Chandra, NMR Relaxation in Tissues With Weak Magnetic
       Inhomogeneities., Magn. Reson. Med. 44 (2000) 144–156.
       http://www.ncbi.nlm.nih.gov/pubmed/10893533.

[51]   A.G. Gardener, S.T. Francis, M. Prior, A. Peters, P.A. Gowland, Dependence of blood R2
       relaxivity on CPMG echo-spacing at 2.35 and 7 T., Magn. Reson. Med. 64 (2010) 967–74.
       doi:10.1002/mrm.22575.

[52]   J.J. Chen, G.B. Pike, Human whole blood T2 relaxometry at 3 Tesla., Magn. Reson. Med.
       61 (2009) 249–54. doi:10.1002/mrm.21858.

[53]   B. Stefanovic, G.B. Pike, Human whole-blood relaxometry at 1.5 T: Assessment of
       diffusion and exchange models., Magn. Reson. Med. 52 (2004) 716–23.
       doi:10.1002/mrm.20218.

Chapter 2

INVESTIGATING THE RELATIONSHIP BETWEEN TRANSVERSE RELAXATION RATE (R_2) AND INTERECHO TIME IN MRI REPORTER GENE-BASED IRON-LABELED CELLS

2.1 Introduction

Gene-based iron-labeling is an emerging method of providing magnetic resonance imaging (MRI) contrast for long-term cell tracking and monitoring of cellular activities [1,2]. Development of this tool could ultimately lead to effective MRI reporter gene expression that enables the non-invasive, in vivo tracking of transcription factor activity. Hence, this technique may provide a valuable tool for studying the underlying mechanisms of tumor growth and metastasis [1,3], as well as for following stem cell migration and differentiation to optimize regenerative stem cell therapy [4]. To achieve gene-based iron-labeling, which in turn leads to increased intracellular levels of iron nanoparticles, several types of iron-handling proteins have been examined [5,6]. Of these, *MagA*, a putative iron transport gene found in magnetotactic bacteria, has been explored in the context of mammalian cell tracking with MRI [2]. Whereas the expression of *MagA* in non-magnetic bacteria like E. coli results in the formation of iron-filled vesicles [7], the exact mechanism of iron storage in mammalian cells has yet to be described [2]. However, enhanced iron accumulation in mammalian cells due to *MagA* expression and iron supplementation has been demonstrated [8,9]. In addition, longitudinal MRI tracking of mouse tumor xenografts from transplanted MagA-expressing cells has been achieved based on analysis of signal voids [1].

Although gene-based contrast shows great promise as a tool for molecular MRI, there are further challenges to overcome in order to achieve optimal utilization. In particular, cellular iron content associated with gene-based labeling is much lower than that obtainable with exogenous agents (e.g., SPIO particles), leading to a weaker effect on the MRI signal. In addition, the influence of cellular iron on the signal of standard MR images is rather non-specific, for example, lowering signal intensity on T2- and T2*-weighted images. Development of more iron-specific quantification tools would help to overcome these challenges. This will entail a more complete

understanding of the influence of iron-labeling on the fundamental MRI parameters, to provide insight into the design of optimal methods for detecting gene-based iron-labeled cells and for further development of these labeling systems.

Amongst various MRI parameters, those that are more specifically influenced by microscopic magnetic field inhomogeneities, such as those created by iron particles as compared to other tissue characteristics, are of particular interest. In a previous work [8], the transverse relaxation rate known as R_2' ($R_2' = R_2^* - R_2$), which is thought to be more strongly influenced by iron than by other tissue properties, was explored. However, one of the limitations of R_2' is its sensitivity to macroscopic field inhomogeneities, although methods for correcting this have been applied. In the present work, we consider a different strategy for assessing iron-related signal, namely, the change in transverse relaxation rate (R_2) with interecho time (2τ) using the Carr-Purcell-Meiboom-Gill (CPMG) sequence [10]. Several studies [10–14] have shown that R_2 increases with increasing interecho time in iron-containing tissues. That is, the decay becomes more irreversible as the refocusing pulses are moved further apart, providing more time during each refocusing interval, for changes in the local magnetic field experienced by protons.

An early mathematical model (the Luz-Meiboom Model) developed to describe changes in R_2 with interecho time was based on fast-exchange between protons in different discrete chemical environments [15]. Although initially derived in the context of a system with multiple chemical environments, the model could apply to multiple physical environments (e.g., compartments with different local magnetic fields). (The application to multiple compartments assumes a common lifetime for all compartments/environments. Refer to the appendix in Luz and Meiboom (1963).) In the context of tissues, this model has been applied to describe the experimental dependence of R_2 on interecho time in various settings, including deoxygenated blood [16–22] and brain tissue [16,23].

More recently, Jensen and Chandra developed a mathematical model describing the R_2 dependence on interecho time based on water diffusion through a microscopic magnetic field spatial distribution [13]. This model relies on an assumed spatial correlation function (eqn. 26 of Jensen and Chandra, 2000) which corresponds to treating the microscopic magnetic field as a random variable of position. Compared to the Luz-Meiboom model, the Jensen-Chandra model [13] provided a better fit to experimental data from iron-containing tissues and deoxygenated red

26

blood cell suspensions, and in more recent studies showed a slightly better fit for human blood samples [18,19]. Despite these findings, it is not clear which model would be superior in other systems such as gene-based iron-labeled cells, in which iron could be distributed differently (i.e., magnetosome, which is a membrane-enclosed compartment of magnetite (Fe_3O_4) [2]) than those previously studied.

In the present study, the relationship between R_2 and interecho time was studied using a 9.4 T nuclear magnetic resonance (NMR) spectrometer in MagA-expressing cells and their untransfected parental control, cultured in the presence and absence of iron-supplemented medium. To our knowledge, this is the first report describing this relationship in cultured cells using gene-based iron-labeling. The relationship between R_2 and interecho time in each cell group was analyzed using both the Luz-Meiboom [15] and the Jensen-Chandra [13] models. Performance of these models was compared for all cell groups. Implications for applying MRI to detect gene-based iron-labeled cells, based on changes in R_2 with interecho time, are also discussed.

2.2 Methods

2.2.1 Cell Preparation

The human tumor cell line, MDA-MB-435, was stably transfected with *MagA* as previously described [24]. A clonal line of MagA-expressing cells (MagA) as well as the untransfected parental cell line (P) were cultured in low glucose Dulbecco's modified Eagle's medium (DMEM) with up to 1% penicillin/streptomycin and 10% fetal bovine serum. All cell culture reagents were purchased from Invitrogen (Carlsbad, CA, USA) unless otherwise noted. MagA expression was maintained with 800 µg/ml Zeocin. Cultures with and without iron supplementation (±Fe) were prepared, providing four experimental cell groups (MagA+Fe, MagA-Fe, P+Fe, and P-Fe). Iron-supplemented cells were incubated in medium containing 250 µM ferric nitrate for a minimum of 5 days. Since we expect the MagA+Fe cells to have the greatest iron uptake, we will refer to the remaining groups (MagA-Fe, P+Fe, and P-Fe) as the "control cells".

At harvest, cells were washed with phosphate buffered saline (PBS) pH 7.4 and counted using a hemacytometer as previously described[8]. Five million cells were placed in a custom-made NMR-compatible vial, with a 2.2 mm inner diameter and centrifuged for 5 min at 400xg and 15°C to form a compact pellet. Excess PBS was removed from the vial by inserting a custom-made plunger to the PBS-pellet boundary. Unused cells were lysed in 850 µl RIPA (10 mM Tris-HCl pH 7.5/140 mM NaCl/1% NP-40/1% sodium deoxycholate/0.1% SDS)/150 µL Complete Mini protease inhibitor cocktail (Roche Diagnostic Systems, Laval, Canada) such that approximately 10 million cells were solubilized per ml of lysis buffer and stored at -20°C for later iron analysis.

2.2.2 Iron Analysis

Trace element analysis of iron was performed by the Analytical Services Laboratory of Western University (London, Canada) using inductively-coupled plasma mass spectrometry (ICP-MS). Protein levels were determined using the BCA assay [25] and were used to normalize iron contents.

2.2.3 NMR Measurement

R_2 measurements, as a function of 2τ, were performed on cell pellets: MagA+Fe (n=5), MagA-Fe (n=3), P+Fe (n=3), and P-Fe (n=3). To assure that any observed changes in R_2 were not due to artifacts from imperfect refocusing pulses, R_2 was also measured as a function of 2τ in 100 µM MnCl$_2$(aq) (n=3). All R_2 measurements were completed within 7 hours of the initial cell harvest.

R_2 was measured on a 9.4 Tesla NMR spectrometer (Varian Inova 400 equipped with the Agilent auto-switchable double resonance coil) using the CPMG sequence provided by the vendor. For this implementation of the CPMG sequence, only a single echo signal was acquired following each train of 180° pulses, with signal acquisition starting at the echo refocusing time. Each echo contributed to a single point on the associated R_2 decay curve. Multiple echo points (8-15 points) on this curve, each at a different signal echo time (TE), were obtained by varying the number of

refocusing pulses in the train while the interecho time was fixed. Here, TE refers to the time between initial excitation and data acquisition. An even number of refocusing pulses was applied in all acquisitions. The procedure was repeated with interecho times (2τ) ranging between 0.2 – 16 ms (TE = 2τ x (number of pulses in the train)). The decay of echo signals were all acquired for 1s with a spectral width of 49751 Hz (dwell time ~ 10 µs) and averaged over an 8 step phase cycling scheme [26]. For all signal acquisition, TR > 2 s (TR = TE + 2 s). On average, the refocusing (RF) pulse duration was 27.2 ± 0.85 µs. All measurements were acquired on-resonance at 25°C.

2.2.4 R_2 Analysis

A linear fit was applied to the time interval between 100 – 1000 µs of each echo signal to determine the signal value for that TE and 2τ. The signal values as a function of TE (8 to 15 echo values for each 2τ) were fitted to a mono-exponential decay function to determine the value of R_2. Individual R_2 values were corrected based on the assumption that signal decay rate has a 2-fold reduction during the time period that each RF pulse was applied [27]. All signal analysis was done using Matlab R2013a (MathWorks, Natick, USA).

2.2.5 Theoretical Models

Two previously developed mathematical models were applied to the experimentally determined R_2 values at various 2τ using the Levenberg-Marquardt algorithm, which searches for the optimal model parameters such that sum of squared errors becomes minimized. The Jensen-Chandra model [13] describes the dependence of R_2 on interecho time (2τ) as,

$$R_2^{tot} = \left(\frac{G_0\gamma^2 r_c^2}{2D}\right) F\left(\frac{4D\tau}{r_c^2}\right) + \frac{1}{T_{20}} \quad , \qquad (2.1)$$

where G_0 is the variance of the microscopically inhomogeneous magnetic field, γ is the proton gyromagnetic ratio, r_c denotes the spatial correlation length associated with the microscopic magnetic field inhomogeneity, D is the diffusion coefficient of water within the cells or tissue,

and $\frac{1}{T_{20}}$ is the transverse relaxation rate in the absence of these microscopic field inhomogeneities. The function F is defined by [13],

$$F(x) = \frac{1}{\sqrt{\pi}} \int_0^\infty dy \, \frac{e^{-y}}{\sqrt{y}} \left[1 - \frac{1}{xy}\tanh xy\right]. \qquad (2.2)$$

The adjustable parameters $(\sqrt{G_0}, \ r_c, \text{ and } \frac{1}{T_{20}})$ were extracted by applying the Jensen-Chandra model to the experimental data, with the value of D held fixed at a constant value that was determined from diffusion coefficient analysis (section 2.2.6). Fitting was also performed using the Luz-Meiboom model [15] cast in a form given by [13],

$$R_2^{tot} = \gamma^2 K_0 \tau_c \left[1 - \frac{\tau_c}{\tau}\tanh\frac{\tau}{\tau_c}\right] + \frac{1}{T_{20}} \quad , \qquad (2.3)$$

where K_0 is the variance of the microscopically inhomogeneous magnetic field, τ_c indicates the exchange time constant, and $\frac{1}{T_{20}}$ is the transverse relaxation rate in the absence of exchange [13]. Similarly, the adjustable parameters $(\sqrt{K_0}, \ \tau_c, \text{ and } \frac{1}{T_{20}})$ were found by applying the Luz-Meiboom model to experimental data.

Goodness of fit was assessed using the coefficient of non-determination $(1 - r^2)$ defined by,

$$1 - r^2 = \frac{SSR}{SST} \quad , \qquad (2.4)$$

where r is the correlation coefficient, SSR is the sum of squared errors and SST is the total sum of squares. In particular, $SSR = \sum_{i=1}^n (f_i - y_i)^2$, $SST = \sum_{i=1}^n (y_i - y_{avg})^2$, where y_i represents the ith experimental data point, f_i is the estimated value of that data point according to the model, and the subscript *avg* represents average. The value of $1 - r^2$ measures the degree of uncertainty in the data that is not explained by the model.

2.2.6 Diffusion Coefficient Analysis

The diffusion coefficient (D) used in eqn. 2.1 was determined from separate diffusion-weighted MRI experiments (Siemens 3T, mMR system) using a standard echo-planar imaging acquisition having the following parameters: single slice, 2mm thick, FOV = 150 x 150 mm, matrix size =

128 x 128; TR = 3000 ms; TE = 94 ms; 8 signal averages; bandwidth along read direction = 977 Hz/pixel, $b = 0$ and $b = 1000$ s/mm^2. Using this sequence, the apparent diffusion coefficient was measured in compact pellets of MagA-expressing cells (n=4).

2.3 Results

Iron content (normalized to protein) measured by ICP-MS is provided in Fig. 2.1. Iron levels are shown for all samples except for two that were not measured: MagA+Fe (1) in Table 2.1 (see also the top curve in Fig. 2.2) and MagA-Fe (1) in Table 2. MagA+Fe samples accumulated more iron than all of the other samples except P+Fe (1), which showed an iron level comparable to those of MagA+Fe. Iron measurement of P+Fe (1) was repeated 3-times to determine a representative standard error of this measurement (approximately 5%). For this particular sample, the mean value was reported in Fig. 2.1.

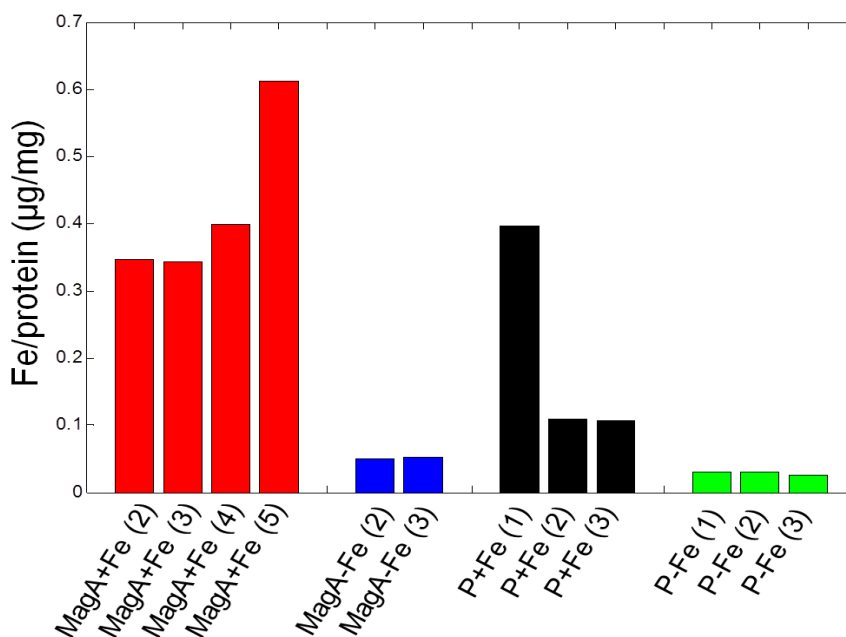**Figure 2.1. Intracellular iron concentration measured by ICP-MS**. Each bar represents the iron measurement from an individual NMR sample. Iron levels were not measured in the samples denoted as MagA+Fe (1) (highest R_2 in Fig. 2.2) and MagA-Fe (1) in Tables 2.1 and 2.2, respectively. Based on triplicate measurement of one sample (P+Fe (1)), there is an approximately 5% standard error of the mean in iron measurement.

For all samples, R_2 increased with increasing 2τ regardless of *MagA* expression or iron-supplementation, with 2τ values ranging from $0.2 - 16$ ms (Fig. 2.2). However, the increase in R_2 with 2τ was stronger in MagA+Fe (n=5) than for control cells (Fig. 2.2). For control cells, R_2 tended to plateau over the 2τ region between $2 - 16$ ms, with changes in R_2 over this region being $< 2s^{-1}$. In contrast, for MagA+Fe cells the change in R_2 over this region ranged from approximately $2 - 7$ s^{-1}. For one of the MagA+Fe samples (MagA+Fe (1), the top curve in Fig. 2.2, no iron level measured), all R_2 values and the change in R_2 with 2τ ($0.2 - 16$ ms) appeared to be substantially higher than for other samples. The normalized signal decay curves in Fig. 2.3 illustrate the difference in the rate of signal decay as 2τ changes in a representative sample of MagA+Fe (highest black circles, Fig. 2.2).
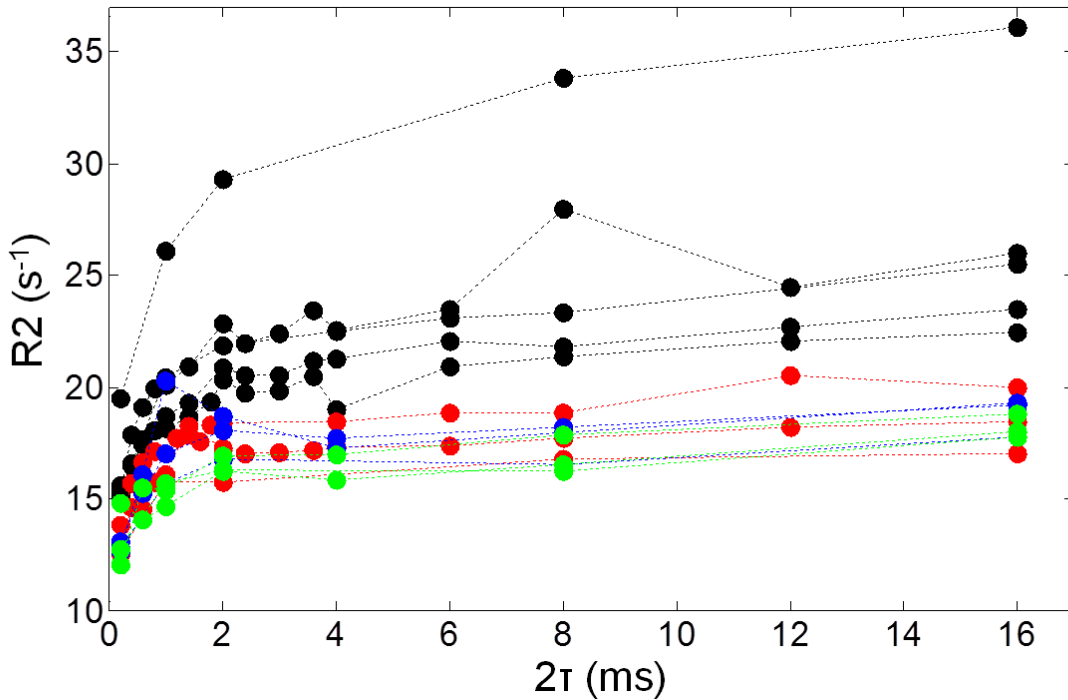
Figure 2.2. Measured R_2 values at various 2τ in MagA+Fe (n=5), MagA-Fe (n=3), P+Fe (n=3), and P-Fe (n=3). MagA+Fe samples are represented with black circles. Control cells (MagA-Fe, P+Fe, and P-Fe, n=3 each) are marked with circles (red, blue, and green, respectively). For individual R_2 values uncertainties (standard errors) were less than 0.25 s^{-1} for all but two individual R_2 values that had uncertainties close to 0.5 s^{-1}.
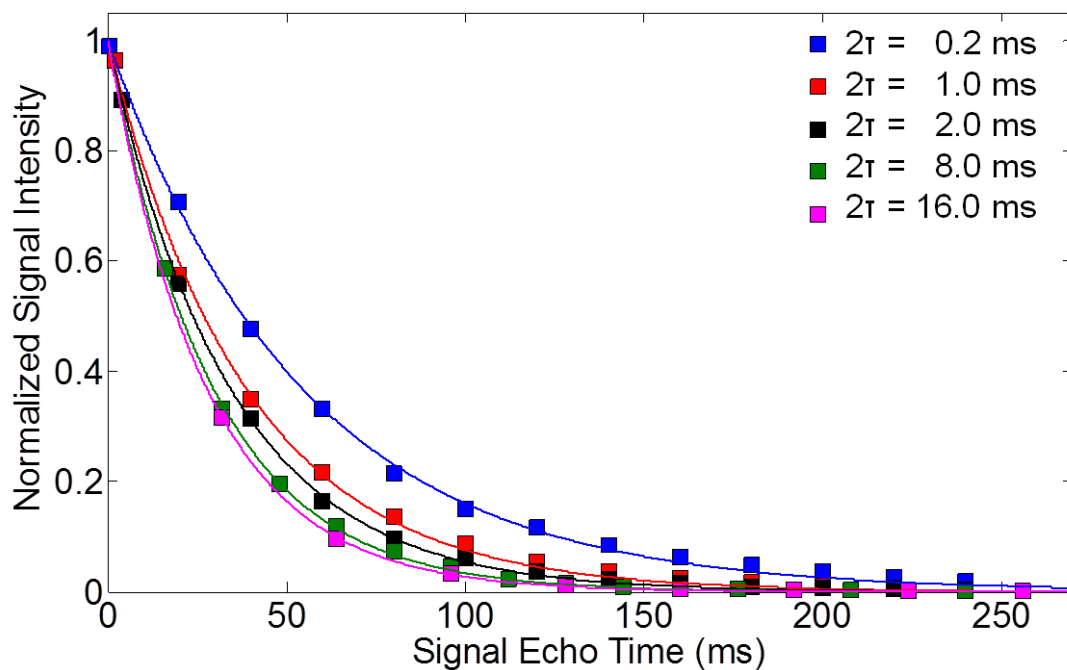
Figure 2.3. The normalized signal intensity decay curves of a representative sample (MagA+Fe (1)) with different values of 2τ. Amplitudes were normalized to have an initial value of 1. The signal intensity decays faster with higher 2τ values compared to lower 2τ.

For 100 μM $MnCl_{2(aq)}$ samples (n=3, Fig. 2.4), variations of R_2 as a function of 2τ were small compared to changes for cell samples (with any deviations at short 2τ being within ± 1 s^{-1} of long 2τ values), indicating that the R_2 variation with 2τ observed in cells was not an artifact associated with increasing number of RF pulses applied with the shorter 2τ values.
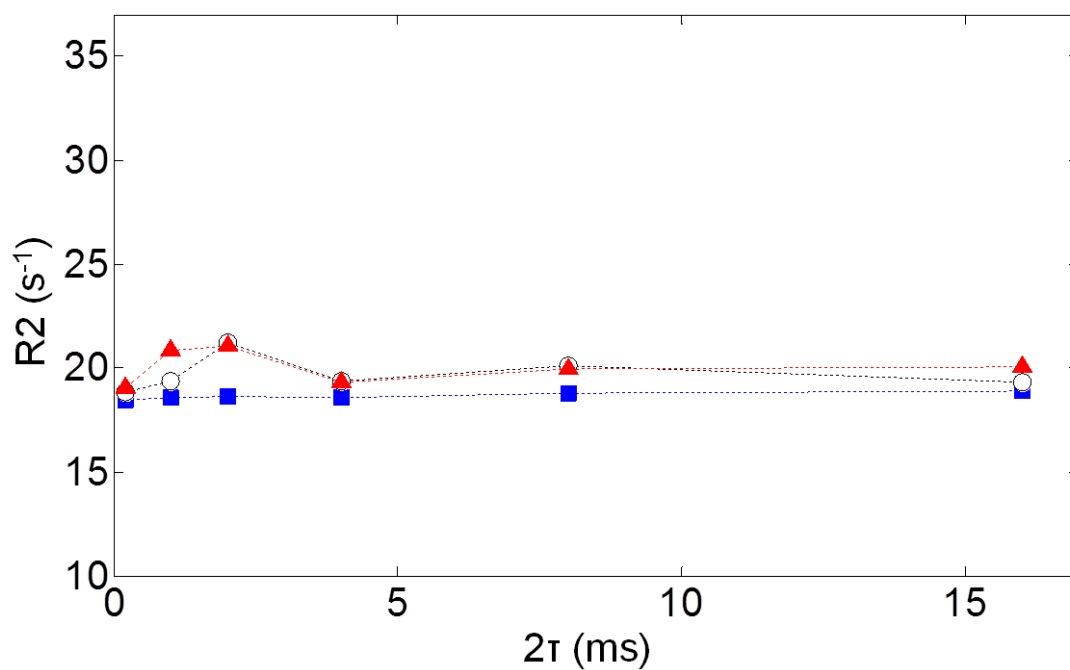
Figure 2.4. Measured R_2 values at various 2τ for 100 μM $MnCl_2$ samples (n=3).

Fig. 2.5 illustrates fitted curves for MagA+Fe (n=5) obtained with the Jensen-Chandra model (solid curves). The Luz-Meiboom model (dashed curves) is also shown for two of the samples. The Jensen-Chandra model provides a better fit than the Luz-Meiboom model, as evaluated by the ratio of the coefficient of non-determination obtained with the Luz-Meiboom model to that of the Jensen-Chandra model ($\frac{1-r^2_{Luz-Meiboom}}{1-r^2_{Jensen-Chandra}}$). This ratio was greater than 1 for all samples (13.4 for the sample with the highest R_2 values (highest black circles in Fig. 2.2) and ranged from 1.4 to 2.7 for the other four samples.)
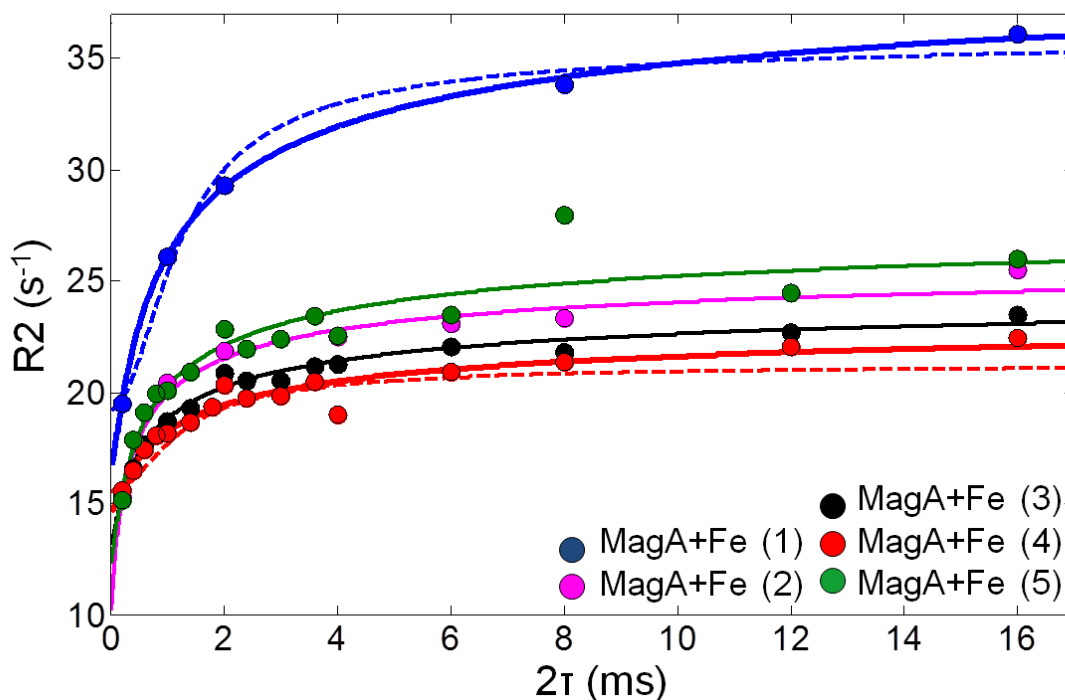
Figure 2.5. Application of the Jensen-Chandra and the Luz-Meiboom models to measured R_2 values in MagA+Fe (n=5). Individual samples are distinguished by different colours. All heavy-weighted curves indicate the Jensen-Chandra model fit to the corresponding samples. The two dashed curves indicate representative fitting to the Luz-Meiboom model.

Model parameters of fit and the coefficients of non-determination $(1 - r^2)$ derived from fitting the Jensen-Chandra model for MagA+Fe samples are listed in Table 2.1. The values of r_c shown assume that $D = 0.55$ μm^2/ms, which is the mean value obtained from diffusion-weighted imaging experiments as explained in Section 2.2.6. (The standard deviation of D was 0.08 μm^2/ms.) Standard errors obtained from the fitting procedures are also provided for each parameter estimated in Table 2.1.

Table 2.1. Model parameters and coefficients of non-determination $(1 - r^2)$ obtained from applying the Jensen-Chandra model to iron-supplemented, MagA-expressing cells[b].

Sample	$\gamma^2 G_0 r_c^2/2D$ (s^{-1})[a]	$\sqrt{G_0}$ (μT)	r_c (μm)[c]	$\frac{1}{T_{20}}$ (s^{-1})	$1 - r^2$
MagA+Fe (1)	24.1 ± 0.6	1.4 ± 0.1	0.44 ± 0.04	16.7 ± 0.7	0.001
MagA+Fe (2)	16.3 ± 2.5	2.1 ± 0.7	0.24 ± 0.07	10.1 ± 2.8	0.026
MagA+Fe (3)	12.0 ± 0.2	1.2 ± 0.1	0.35 ± 0.02	13.1 ± 0.3	0.015
MagA+Fe (4)	9.4 ± 0.2	0.8 ± 0.1	0.45 ± 0.03	14.6 ± 0.3	0.064
MagA+Fe (5)	16.1 ± 0.9	1.5 ± 0.2	0.33 ± 0.04	12.3 ± 1.1	0.101

[a] $\gamma^2 G_0 r_c^2/2D$ represents the total amplitude of a curve.
[b] The model parameters for control cells are not shown as the Jensen-Chandra model was not considered as a reasonable fit to these group.
[c] The r_c values were calculated assuming $D = 0.55$ μm^2/ms, which was determined from diffusion coefficient analysis (section 2.2.6)

Fig. 2.6 illustrates curves obtained from fitting the Luz-Meiboom model to representative samples from each sub-group of control cells (MagA-Fe, P+Fe, and P-Fe). The fitted curves from the Jensen-Chandra model are not shown as these provided, in most cases, non-physical parameter estimates ($\frac{1}{T_{20}} < 0$, for seven samples and $\frac{1}{T_{20}}$ was within one standard error of zero for an eighth sample); therefore, the Jensen-Chandra model was not considered as a reasonable representation of this data. Model parameters of fit and the coefficients of non-determination ($1 - r^2$) derived from applying the Luz-Meiboom model to all samples are summarized in Table 2.2. Model parameters for one of the P+Fe samples (P+Fe (3)) is not provided in Table 2.2 since fitting to either Luz-Meiboom or Jensen Chandra model provided a non-physical parameter ($\frac{1}{T_{20}} < 0$). Similarly, model parameters ($\sqrt{K_0}$ and τ_c) for one of the samples (P-Fe (2)) differs greatly from those of the other samples. This is likely associated with the large deviation of R_2 at $2\tau = 0.2$ ms (Fig. 2.2). The values of $\frac{1}{T_{20}}$ for these control cells were not significantly different than those of MagA+Fe cells determined using the Jensen-Chandra model ($t = 0.37$, $p < 0.05$, two-tailed). The values of $\frac{1}{T_{20}}$ for MagA+Fe cells that were determined using the Luz-Meiboom model were higher but comparable to that obtained for control cells (Table 2.2).
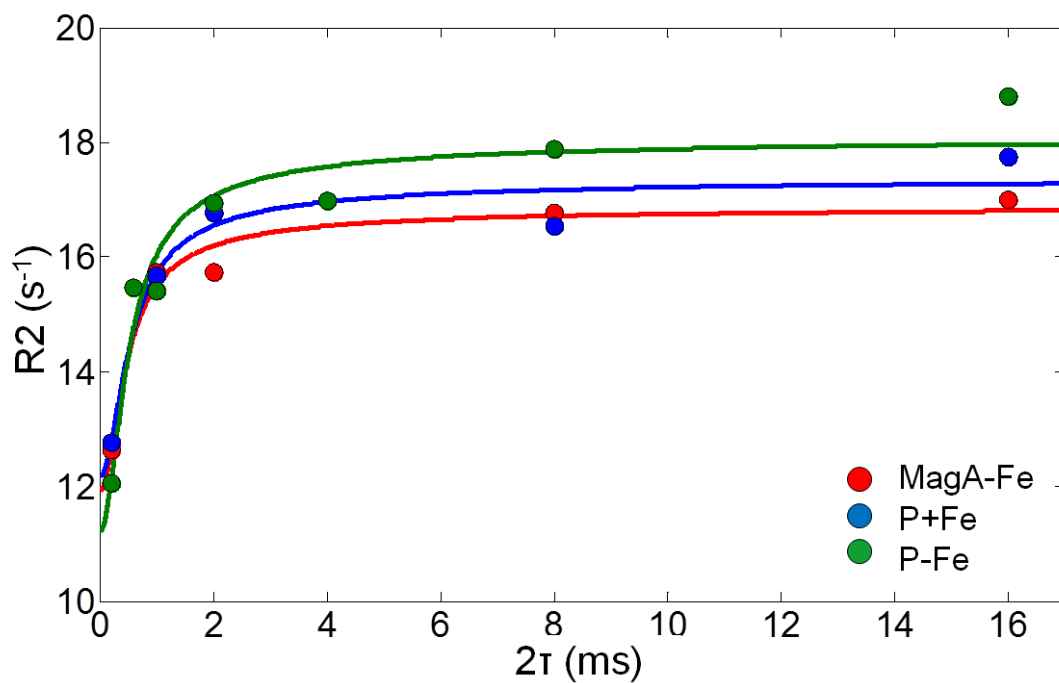
Figure 2.6. Application of the Luz-Meiboom model to measured R_2 values in controls. Solid curves represent the Luz-Meiboom model applied to representative samples from MagA-Fe (red), P+Fe (blue), and P-Fe (green). Note the difference in the scales of y-axis from Figures 2.2, 2.4 and 2.5.

Table 2.2. Model parameters and coefficients of non-determination $(1 - r^2)$ obtained from applying the Luz-Meiboom model to all cell samples[a].

Sample	$\gamma^2 K_0 \tau_c$ (s^{-1})[b]	$\sqrt{K_0}$ (μT)	τ_c (ms)	$\frac{1}{T_{20}}$ (s^{-1})	$1 - r^2$
MagA+Fe (1)	16.8 ± 1.4	0.81 ± 0.08	0.36 ± 0.06	19.2 ± 1.1	0.01
MagA+Fe (2)	9.6 ± 0.6	0.76 ± 0.07	0.23 ± 0.04	14.8 ± 0.6	0.05
MagA+Fe (3)	7.3 ± 0.1	0.57 ± 0.01	0.31 ± 0.01	15.1 ± 0.1	0.04
MagA+Fe (4)	5.8 ± 0.2	0.47 ± 0.02	0.36 ± 0.02	15.6 ± 0.2	0.11
MagA+Fe (5)	9.4 ± 0.4	0.66 ± 0.03	0.30 ± 0.03	15.9 ± 0.4	0.14
MagA-Fe (1)	5.0 ± 0.8	0.71 ± 0.18	0.14 ± 0.07	11.9 ± 0.9	0.03
MagA-Fe (2)	6.0 ± 0.2	0.68 ± 0.03	0.18 ± 0.01	13.5 ± 0.2	0.09
MagA-Fe (3)	6.3 ± 0.3	0.79 ± 0.04	0.14 ± 0.01	11.7 ± 0.3	0.10
P+Fe (1)	5.2 ± 1.0	0.68 ± 0.20	0.16 ± 0.08	12.2 ± 1.0	0.05
P+Fe (2)	6.5 ± 0.4	0.75 ± 0.06	0.16 ± 0.02	12.4 ± 0.4	0.04
P-Fe (1)	5.0 ± 1.2	0.67 ± 0.25	0.16 ± 0.11	12.1 ± 1.2	0.07
P-Fe (2)	3.4 ± 0.4	0.23 ± 0.04	0.93 ± 0.29	14.5 ± 0.2	0.18
P-Fe (3)	6.9 ± 0.6	0.81 ± 0.09	0.15 ± 0.03	11.2 ± 0.7	0.07

[a] Results for P+Fe (3) are not reported because the fitting to either the Luz-Meiboom or the Jensen Chandra model provided a non-physical parameter ($\frac{1}{T_{20}} < 0$).

[b] $\gamma^2 K_0 \tau_c$ represents the total amplitude of a curve.

2.4 Discussion

In this paper, we have demonstrated and quantified the dependence of the transverse relaxation rate (R_2) on interecho time in MagA-expressing cells and the corresponding parental cell line. To our knowledge, this is the first report to investigate this dependence in gene-based iron-labeled cells. The relationship between R_2 and interecho time was further characterized with previously developed mathematical models, providing quantitative estimates of parameters thought to be associated with MR relaxation mechanisms. In the future, this type of analysis could be applied to compare different gene-based iron-labeled systems and may help to guide their further development for reporter gene expression using MRI.

2.4.1 Iron Content

The iron levels reported here can be directly compared to those previously reported [8] for iron-supplemented MagA-expressing cells of the same type cultured under the same iron-supplemented conditions (250 µM ferric nitrate). These authors [8] reported a mean iron level of 0.67 ± 0.11 µg Fe/(mg of protein) which is comparable to values reported here (Fig. 2.1). It should also be noted that our values in Fig. 2.1 do not include levels for one of our samples (highest black circles in Fig. 2.2) which may have had the highest iron content of our samples. Although magnetosomes can be formed in the absence of *MagA* expression [28,29], other reports and our iron content analysis showed that *MagA* over-expression results in an increased level of cellular iron [8,9].

We calculated the iron content per cell, to compare our results to estimates reported in other studies of gene-based iron labeling. In our samples, there were approximately 370 million cells per ml (based on pellet volume and number of cells in the pellet) and we assumed that protein accounts for approximately 20% of total cell weight [30] and that the mass density of samples is approximately 1.0 g/ml. This leads to an estimate of $0.19 - 0.33$ pg Fe/cell for our MagA+Fe samples which is comparable to iron levels (0.59 ± 0.14 pg/cell) found in another MagA-expressing mammalian cell line cultured in the presence of 200 µM ferric citrate [9].

To compare our iron levels to values reported for tissue, we again assumed that protein accounts for approximately 20% of total cell weight [30]. This leads to estimated iron levels per unit mass of pellet of $0.07 - 0.12$ µg Fe/mg, for our MagA+Fe samples, which is comparable to human brain iron levels ($0.05 - 0.21$ µg Fe/mg) and levels in human liver (0.13 µg Fe/mg) [31]. Interestingly, iron levels are quite low (0.02 µg Fe/mg) in the mouse brain [32], which is advantageous for cell tracking, in contrast to other mouse organs (0.21 µg Fe/mg of liver, 0.11 µg Fe/mg of heart, and 0.14 µg Fe/mg of kidney [33]).

2.4.2 Analysis Using the Jensen-Chandra and the Luz-Meiboom Models

The curves shown in Fig. 2.5 suggest that the relationship between R_2 and 2τ for MagA+Fe samples is better described by the Jensen-Chandra model than the Luz-Meiboom model. This is

supported by our reported ratios of $1 - r^2$ and the previous assessment of Jensen and Chandra (2000) in iron-containing tissues [13]. The superior performance of the Jensen-Chandra model as well as the apparently mono-exponential shape of the R_2 decay curves (Fig. 2.3) provide support that this model, which depends on the weak field approximation [13], is appropriate for iron-supplemented MagA-expressing systems.

It is interesting that the spatial correlation lengths (r_c) for MagA+Fe samples tended to be smaller than those previously found for iron-containing tissues. Our values of r_c (Table 2.1) ranged between $0.24 - 0.45$ µm, whereas r_c values of $2.3 - 3.1$ µm were measured for regions of human brain, and 0.9 µm for liver [13]. The larger r_c values obtained for brain tissue may reflect larger distances between iron-containing cells (compared to compact cell pellets) since, in gray matter of brain, iron is not uniformly distributed in all cells but is highest in oligodendrocytes [34]. Given this argument, it is possible that in-vivo r_c from implanted MagA –expressing cells might vary depending on the distribution of MagA-expressing cells in each voxel.

We can also compare our values of the root-mean-square field inhomogeneity ($\sqrt{G_0}$) for MagA+Fe cells ($0.8 - 2.1$ µT, Table 2.1) to values obtained from tissue. A previous work [13] that applied the Jensen-Chandra model to data acquired at 2.35 T from brain regions (caudate, putamen, thalamus), with iron contents ($0.08 - 0.12$ µg Fe/mg) similar to our MagA+Fe samples ($0.07 - 0.12$ µg Fe/mg, see above), yielded $\sqrt{G_0}$ values ranging from $0.10 - 0.13$ µT. Assuming a linear relationship between $\sqrt{G_0}$ and field strength, this corresponds to a range of 0.40 to 0.52 µT which is lower than, but of similar order of magnitude as our values. (A linear relationship is reasonable based on room temperature magnetometry data from ferritin samples [35].) Finally, a $\sqrt{G_0}$ value of approximately 1 µT was obtained from rat liver at 8.4 T [13].

The value of $\sqrt{G_0}$ obtained for MagA+Fe cells were higher than $\sqrt{K_0}$ value obtained for the same samples ($0.47 - 0.81$ µT, Table 2.2), which is due, partially, to the lower amplitudes provided by the Luz-Meiboom model fit compared to those from the Jensen-Chandra model. As the Jensen-Chandra model provided a better fit, this model and its parameter ($\sqrt{G_0}$) may be a better estimate of root-mean-square field inhomogeneity of MagA+Fe cells than that found with the Luz-Meiboom model.

Although the Jensen-Chandra model performs well for MagA+Fe samples, it fails to characterize the relationship between R_2 and 2τ in control cells; whereas, the Luz-Meiboom model does fit this data reasonably well. This difference in model fitting is consistent with the visual appearance of the R_2 vs. 2τ curves, which indicates a difference in shape for the control cells compared to the MagA+Fe cells. The control cell curves increase sharply in the short 2τ region (≤ 2 ms), and then almost plateau; whereas, for MagA+Fe the curves show a more gradual increases in the longer 2τ region. The reasons for the better performance of the Luz-Meiboom model for the control cells are unclear. Possibly, iron within these cells is not uniformly distributed at the microscopic level (i.e.,clustered), making a compartment model more appropriate. Also given that, in comparison to the MagA+Fe samples, some of the control cells have rather low iron levels (~0.05 µg Fe/(mg of protein), Fig. 2.1), it is possible that noniron related sources of microscopic field inhomogeneities (associated with microscopic magnetic susceptibility variations) contribute to the change in R_2 with 2τ. An estimate of such a noniron effect is provided by previous experiments with lipoprotein micelles [36]. The authors found that by changing the lipoprotein core radius from approximately 50 $\overset{\circ}{A}$ to 200 $\overset{\circ}{A}$, the frequency of protons inside the core varied over approximately 0.05 ppm, and this was shown to be consistent with predictions based on magnetic susceptibility anisotropy of the shell. This frequency shift (0.05 ppm) would correspond to a microscopic magnetic field shift of approximately 0.5 µT at our field strength (9.4 T), which is of similar order of magnitude as our values of $\sqrt{K_0}$ (Table 2.2). Our values of the exchange rate (τ_c) for control cells are approximately an order of magnitude smaller than typical values obtained from applying the Luz-Meiboom model to blood samples [19]. Similarly, τ_c values for MagA+Fe samples were higher but comparable to that obtained for control cells. Perhaps the faster exchange times for our samples reflects exchange between intracellular "compartments" (i.e., where the distance between compartments is small), whereas with blood, exchange may occur between red blood cells and plasma.

2.4.3 Limitations and Unexplained Observations

As shown in Fig. 2.2, R_2 values for one of our MagA+Fe cells were quite high compared to those of the other four samples. Although it is possible that this could be, in part, due to higher iron

levels in this sample, this possibility cannot be confirmed because an iron measurement was not carried out for this sample. However, iron levels as high as 1.4 µg Fe/(mg of protein) have been obtained from iron supplemented MagA-expressing cells of the same type cultured under the same iron-supplemented conditions [37]. Variability in MRI-based R_2 measurements from these previously studied samples was associated with variability in iron levels based on correlation analysis [37].

Although the difference in shape and lower amplitude of the R_2 versus 2τ data for control samples compared to MagA+Fe samples seems reasonable based on the lower iron levels of the former, this does not explain the observations for one of the control samples (P+Fe (1)). For this sample, the R_2 versus 2τ data (including model fitting) was similar to those of the other control cells despite the high iron levels (Fig. 2.1). Although the explanation for this is not clear, one might speculate that a high level of iron remained in this sample due to a transient fluctuation in iron homeostasis [38] that is not representative of the major form of iron found in MagA+Fe samples.

For our R_2 measurements at the shortest 2τ value (0.2 ms), the time duration of each refocusing RF pulse was approximately 12 % of the total interecho time (2τ). While B_1 is on, the magnetization component along B_1 should decay with a rate of $1/T_{1\rho}$ (rather than R_2), influencing the net decay rate over the complete pulse train (signal echo time). We corrected for this effect based on the previously obtained theoretical result [27], which indicates that the decay rate during the RF pulse is reduced by a factor of two [27]. (This correction factor is valid as long as the rate of precession about $B_1 \gg R_2^*$.) A different approach for this correction would be to measure $1/T_{1\rho}$ at the spin-locking B_1 value applied for the refocusing RF pulses used in the CPMG sequence. (This would require an RF coil that can withstand such high amplitudes for tens to hundreds of milliseconds.)

In addition, measurement of the R_2 versus 2τ relationship can, in principle, be confounded by the changes in R_2 decay curve sampling that naturally occur with increasing 2τ. For this work, in which an even number of refocusing pulses was applied, the earliest sample was collected at a signal echo time of 4τ and hence regions of the curve at times less than 4τ were not observed. This issue is apparent on the R_2 decay curve for $2\tau = 16$ ms (Fig. 2.3) where the first data point is

located at a signal echo time of 32 ms, which is approximately equal to the T_2 $(1/ R_2)$ for that curve.

2.4.4 Implications for MRI Acquisition

Previously, the 2τ dependence of R_2 has been utilized to provide assessment of iron levels in human brain in-vivo [11,39]. Using three acquisitions, one with a train of refocusing pulses for magnetization preparation, a second with one refocusing pulse for preparation and a third with no preparation, the authors were able to determine the difference between R_2 at two values of 2τ (6 ms and 60 ms in their application). Perhaps, a similar scheme could be used to detect MagA-expressing cells for *in vivo* small animal imaging. For this type of acquisition, our data suggest a minimum 2τ not shorter than 2 ms to avoid confounding the R_2 difference measurement with potentially non-iron related contributions.

2.5 Conclusion

Our NMR studies of iron-supplemented, MagA-expressing cells demonstrated that the dependence of R_2 on intercho time is well-described by the Jensen-Chandra weak field model. The spatial correlation lengths for iron-supplemented, MagA-expressing cells tended to be smaller than those previously obtained from human tissues, and the root-mean-square values of the field inhomogeneity for these cells tended to be slightly larger than in the tissues. Non-supplemented MagA-expressing cells and their parental controls also showed observable changes in R_2 with interecho time, but this was largely at short (< 2 ms) interecho times; whereas, variation in R_2 at longer intercho times was larger for iron-supplemented MagA expressing cells. Interestingly, for non-supplemented MagA-expressing cells and the parental controls, the Luz-Meiboom model provided a more reasonable fit than the Jensen-Chandra model, suggesting a difference in the microscopic magnetic field distribution in these samples relative to the iron-supplemented, MagA-expressing cells. The exchange times obtained from these control samples using the Luz-Meiboom model appear to be approximately an order of magnitude larger than

those of blood samples, suggesting the possibility that dependence of R_2 on interecho time for these samples could be associated with intracellular proton exchange.

2.6 Acknowledgement

2.7 References

[1]   R. Rohani, R. Figueredo, Y. Bureau, J. Koropatnick, P. Foster, R.T. Thompson, et al., Imaging Tumor Growth Non-invasively Using Expression of MagA or Modified Ferritin Subunits to Augment Intracellular Contrast for Repetitive MRI., Mol. Imaging Biol. 16 (2014) 63–73. doi:10.1007/s11307-013-0661-8.

[2]   D.E. Goldhawk, R. Rohani, A. Sengupta, N. Gelman, F.S. Prato, Using the magnetosome to model effective gene-based contrast for magnetic resonance imaging., Wiley Interdiscip. Rev. Nanomed. Nanobiotechnol. 4 (2012) 378–88. doi:10.1002/wnan.1165.

[3]   C. Mees, J. Nemunaitis, N. Senzer, Transcription factors: their potential as targets for an individualized therapeutic approach to cancer., Cancer Gene Ther. 16 (2009) 103–12. doi:10.1038/cgt.2008.73.

[4]   M. Vandsburger, Cardiac Cell Tracking with MRI Reporter Genes: Welcoming a New Field., Curr. Cardiovasc. Imaging Rep. 7 (2014) 9250. doi:10.1007/s12410-013-9250-0.

[5]   B. Iordanova, E.T. Ahrens, In vivo magnetic resonance imaging of ferritin-based reporter visualizes native neuroblast migration., Neuroimage. 59 (2012) 1004–12. doi:10.1016/j.neuroimage.2011.08.068.

[6] A.E. Deans, Y.Z. Wadghiri, L.M. Bernas, X. Yu, B.K. Rutt, D.H. Turnbull, Cellular MRI contrast via coexpression of transferrin receptor and ferritin., Magn. Reson. Med. 56 (2006) 51–9. doi:10.1002/mrm.20914.

[7] C. Nakamura, J.G. Burgess, K. Sode, T. Matsunaga, An Iron-regulated Gene, magA, Encoding an Iron Transport Protein of Magnetospirillum sp. Strain AMB-1, J. Biol. Chem. 270 (1995) 28392–28396. doi:10.1074/jbc.270.47.28392.

[8] A. Sengupta, K. Quiaoit, R.T. Thompson, F.S. Prato, N. Gelman, D.E. Goldhawk, Biophysical features of MagA expression in mammalian cells: implications for MRI contrast., Front. Microbiol. 5 (2014) 1–9. doi:10.3389/fmicb.2014.00029.

[9] O. Zurkiya, A.W.S. Chan, X. Hu, MagA is sufficient for producing magnetic nanoparticles in mammalian cells, making it an MRI reporter., Magn. Reson. Med. 59 (2008) 1225–31. doi:10.1002/mrm.21606.

[10] J. Vymazal, R. a Brooks, N. Patronas, M. Hajek, J.W. Bulte, G. Di Chiro, Magnetic resonance imaging of brain iron in health and disease., J. Neurol. Sci. 134 Suppl (1995) 19–26. http://www.ncbi.nlm.nih.gov/pubmed/8847541.

[11] F.Q. Ye, W.R. Wayne Martin, P.S. Allen, Estimation of the iron concentration in excised gray matter by means of proton relaxation measurements., Magn. Reson. Med. 35 (1996) 285–9. http://www.ncbi.nlm.nih.gov/pubmed/8699938.

[12] A. Hocq, N. Brouette, S. Saussez, M. Luhmer, P. Gillis, Y. Gossuin, Variable-field relaxometry of iron-containing human tissues: a preliminary study., Contrast Media Mol. Imaging. 4 (2009) 157–64. doi:10.1002/cmmi.275.

[13] J.H. Jensen, R. Chandra, NMR Relaxation in Tissues With Weak Magnetic Inhomogeneities., Magn. Reson. Med. 44 (2000) 144–156. http://www.ncbi.nlm.nih.gov/pubmed/10893533.

[14] J. Vymazal, R.A. Brooks, C. Baumgarner, V. Tran, D. Katz, J.W.M. Bulte, et al., The relation between brain iron and NMR relaxation times: an in vitro study, Magn. Reson. Med. 35 (1996) 56–61.

[15] Z. Luz, S. Meiboom, Nuclear Magnetic Resonance Study of the Protolysis of Trimethylammonium Ion in Aqueous Solution—Order of the Reaction with Respect to Solvent, J. Chem. Phys. 39 (1963) 366–370. doi:10.1063/1.1734254.

[16] R.A. Brooks, J. Vymazal, J.W. Bulte, C.D. Baumgarner, V. Tran, Comparison of T2 Relaxation in Blood, Brain, and Ferritin, J. Magn. Reson. Imaging. 5 (1995) 446–450.

[17] K.R. Thulborn, J.C. Waterton, P.M. Matthews, G.K. Radda, Oxygenation dependence of the transverse relaxation time of water protons in whole blood at high field, Biochim. Biophys. Acta. 714 (1982) 265–270.

[18] J.J. Chen, G.B. Pike, Human whole blood T2 relaxometry at 3 Tesla., Magn. Reson. Med. 61 (2009) 249–54. doi:10.1002/mrm.21858.

[19] A.G. Gardener, S.T. Francis, M. Prior, A. Peters, P.A. Gowland, Dependence of blood R2 relaxivity on CPMG echo-spacing at 2.35 and 7 T., Magn. Reson. Med. 64 (2010) 967–74. doi:10.1002/mrm.22575.

[20] M.E. Meyer, O. Yu, B. Eclancher, D. Grucker, J. Chambron, NMR relaxation rates and blood oxygenation level., Magn. Reson. Med. 34 (1995) 234–41. http://www.ncbi.nlm.nih.gov/pubmed/7476083.

[21] B. Stefanovic, G.B. Pike, Human whole-blood relaxometry at 1.5 T: Assessment of diffusion and exchange models., Magn. Reson. Med. 52 (2004) 716–23. doi:10.1002/mrm.20218.

[22] F.Q. Ye, P.S. Allen, Relaxation enhancement of the transverse magnetization of water protons in paramagnetic suspensions of red blood cells., Magn. Reson. Med. 34 (1995) 713–20. http://www.ncbi.nlm.nih.gov/pubmed/8544692.

[23] B. Stefanovic, J.G. Sled, G.B. Pike, Quantitative T2 in the occipital lobe: the role of the CPMG refocusing rate., J. Magn. Reson. Imaging. 18 (2003) 302–9. doi:10.1002/jmri.10360.

[24] D.E. Goldhawk, C. Lemaire, C.R. Mccreary, R. Mcgirr, S. Dhanvantari, R.T. Thompson, et al., Magnetic Resonance Imaging of Cells Overexpressing MagA , an Endogenous Contrast Agent for Live Cell Imaging, Mol. Imaging. 8 (2009) 129–139. doi:10.2310/7290.2009.00006.

[25] P.K. Smith, R.I. Krohn, G.T. Hermanson, A.K. Mallia, F.H. Gartner, M.D. Provenzano, et al., Measurement of Protein Using Bicinchoninic Acid, Anal. Biochem. 150 (1985) 76–85.

[26] S. Berger, S. Braun, 200 and More NMR Experiments, in: Wiley-VCH, Wienheim, 2004: pp. 164–166.

[27] I. Barnaal, D and Lowe, Effects of Rotating Magnetic Fields on Free-Induction Decay Shapes, Phys. Rev. Lett. 11 (1963) 258–260.

[28] R. Uebe, V. Henn, D. Schüler, The MagA protein of Magnetospirilla is not involved in bacterial magnetite biomineralization., J. Bacteriol. 194 (2012) 1018–23. doi:10.1128/JB.06356-11.

[29] I. Kolinko, A. Lohße, S. Borg, O. Raschdorf, C. Jogler, Q. Tu, et al., Biosynthesis of magnetic nanostructures in a foreign organism by transfer of bacterial magnetosome gene clusters., Nat. Nanotechnol. 9 (2014) 193–7. doi:10.1038/nnano.2014.13.

[30] H. Lodish, A. Berk, S. Zipursky, P. Matsudaira, D. Baltimore, J. Darnell, Molecular Cell Biology, in: 4th editio, W. H. Freeman, New York, 2000. http://www.ncbi.nlm.nih.gov/books/NBK21473/.

[31] B. Hallgren, P. Sourander, The effect of age on the non-haemin iron in the human brain., J. Neurochem. 3 (1958) 41–51. http://www.ncbi.nlm.nih.gov/pubmed/13611557.

[32] D.J. Hare, J.K. Lee, A.D. Beavis, A. van Gramberg, J. George, P.A. Adlard, et al., Three-dimensional atlas of iron, copper, and zinc in the mouse cerebrum and brainstem., Anal. Chem. 84 (2012) 3990–7. doi:10.1021/ac300374x.

[33] Z. Wang, Y. Yan, Y. Jiang, W. Li, X. Hu, B. Fu, et al., Effect of orally administered hydroxypropyl chitosan on the levels of iron, copper, zinc and calcium in mice., Int. J. Biol. Macromol. 64 (2014) 25–9. doi:10.1016/j.ijbiomac.2013.11.016.

[34] J.R. Connor, S.L. Menzies, S.M. St Martin, E.J. Mufson, Cellular distribution of transferrin, ferritin, and iron in normal and aged human brains., J. Neurosci. Res. 27 (1990) 595–611. doi:10.1002/jnr.490270421.

[35] R.A. Brooks, J. Vymazal, R.B. Goldfarb, J.W.M. Bulte, P. Aisen, Relaxometry and Magnetometry of Ferritin, Magn. Reson. Med. 40 (1998) 227–235.

[36] J. Lounila, M. Ala-Korpela, J. Jokisaari, Effects of Orientational Order and Particle Size on the NMR Line Positions of Lipoproteins, Phys. Rev. Lett. 72 (1994) 4049–4052.

[37] A. Sengupta, MRI Relaxation Rates: A Quantitative Approach to Track Tumour Cells Expressing MagA (MSc Thesis), 2014.

[38] N.C. Andrews, P.J. Schmidt, Iron homeostasis., Annu. Rev. Physiol. 69 (2007) 69–85. doi:10.1146/annurev.physiol.69.031905.164337.

[39] W.R. Martin, F.Q. Ye, P.S. Allen, Increasing striatal iron content associated with normal aging., Mov. Disord. 13 (1998) 281–6. doi:10.1002/mds.870130214.

Chapter 3

SUMMARY AND FUTURE WORK

3.1 Summary of Findings

Developing an iron-specific MR parameter is difficult to achieve but necessary in order to improve the detection of gene-based iron-labeled cells using MRI. A few studies have reported the R_2 dependence on interecho time (2τ) using the CPMG sequence in iron-containing tissues. However, this relationship has not been previously analyzed in the context of gene-based, iron-labeled cells. This thesis has investigated the relationship between R_2 and 2τ in iron- and non-supplemented, MagA-expressing cells and the associated parental tumor cell line (human MDA-MB-435) using NMR. Furthermore, theoretical models by Luz and Meiboom (1963) [1] and Jensen and Chandra (2000) [2], based on fast-exchange and water diffusion, respectively, were applied to the experimental results. Potential contributions to the relationship between R_2 and 2τ in iron-dependent and –independent aspects have been analyzed by comparing how well these two models fit the experimentally obtained R_2 versus 2τ values in gene-based, iron-labeled cells.

The dependence of R_2 on 2τ in all cell groups was measured using a 9.4 T NMR spectrometer and the CPMG sequence. Visually, the curves that illustrated the increase R_2 as a function of 2τ in MagA+Fe samples appear to have a similar shape to those observed in other iron-containing tissues [3–11]. Likewise, the increase in R_2 with increasing 2τ was seen in control cells (MagA-Fe, P+Fe, and P-Fe). However, the amplitude of curves were smaller and R_2 reached a plateau at an earlier 2τ value (~ 2 ms) in control cells compared to that observed in MagA+Fe samples. Overall, the relationship between R_2 and 2τ for MagA+Fe was clearly distinguishable by visual inspection from that of the control cells. In particular, one MagA+Fe sample showed even greater increase in R_2 compared to the rest of MagA+Fe samples. Unfortunately, the iron level of this particular sample was not acquired, limiting the further inspection on the possible cause behind this exceptionally large R_2 increase.

In order to quantitatively assess the relationship between R_2 and 2τ in these cell groups, theoretical models by Luz and Meiboom (1963) [1] and by Jensen and Chandra (2000) [2] were

applied to experimental data. The performance of each model on each cell group was compared using the coefficient of non-determination $(1 - r^2)$. For MagA+Fe, both models fit the experimental data. The value of $1 - r^2$ indicated that the Jensen-Chandra model provided a better fit to MagA+Fe data than the Luz-Meiboom model. Of the Jensen-Chandra model parameters, the spatial correlation length (r_c) in cell samples was smaller than that previously found in other iron-containing tissues, and is consistent with the faster increase in R_2 at shorter 2τ range in cell samples compared to iron-containing tissues. On the other hand, only the Luz-Meiboom model fit the control cell data. The Jensen-Chandra model failed to be a reasonable fit for most of these control samples, providing non-physical model parameters ($\frac{1}{T_{20}} < 0$) as reported in Chapter 2.

In addition to NMR studies, elemental iron analysis was carried out using ICP-MS. Intracellular iron levels in MagA-expressing cells were found to be comparable to those previously reported by Sengupta *et al*. [12]. Among our samples, iron levels in all MagA +Fe samples were higher than the levels in all but one of the control cell samples, which had a comparable iron level to that of MagA+Fe samples.

Based on the very small iron levels in most of the control cells, the increase in R_2 with increasing 2τ appears to be larger than what one would expect. This observation suggests the possibility of an iron-independent effect (e.g., microscopic magnetic susceptibility change effect associated with cellular membranes), in addition to an iron-dependent effect, that contribute to the relationship between R_2 and 2τ observed in gene-based, iron-labeled cells.

While these findings are interesting, there are limitations in observing the relationship between R_2 and 2τ in complex systems such as tissues and genetically-engineered cells. For one, the sharpest increase in R_2 with increasing 2τ occurred at the short 2τ ranges (i.e., on the order of a few ms) in all cell samples, which makes it more challenging to detect these changes with MRI. Potentially, these changes can be detected using a small animal MRI but may require the use of magnetization preparation [13,14]. On the other hand, in iron-containing tissues, the increase in R_2 tends to occur over a longer range of 2τ, allowing easier detection with MRI, even in humans.

3.2 Future Work

Further work may involve addressing the variability in measured R_2 values among cell samples. In this work, one MagA+Fe sample was found to provide much higher R_2 values compared to the remaining samples of MagA+Fe. Unfortunately, iron analysis of this sample was not performed. Intracellular iron measurement for this particular sample would have been informative as this was an outlier that provided the highest R_2 versus 2τ response, i.e., the strongest potential for detection in-vivo. A previous work [15] that also measured the iron contents of MagA+Fe samples, prepared under the same conditions as our study, found that two of the samples (from total of seven samples) had iron contents that were approximately 1.4 μg Fe/mg protein whereas the remaining five samples had values close to those reported here (~ 0.4 - 0.6 μg Fe/mg protein). Based on this previous finding, we can speculate that the particularly high R_2 values for one of my MagA+Fe samples may have been due to high iron levels in that sample. Thus, further work should be done to better characterize the iron level variation, and to understand the sources of such variation in iron-supplemented, MagA-expressing cells (and in parental controls). The ultimate goal of this would be to determine how to obtain the highest iron levels consistently in such samples.

As additional NMR experiments are performed, more R_2 measurement at lower 2τ range may be acquired as our data suggests that most changes in R_2 occur at lower 2τ regime. Additional R_2 data in this region may provide a more ideal representation of R_2 versus 2τ curves, which could also increase the strength of fitting as the theoretical models are applied to the experimental data.

Future work may also involve assessing the influence of constraining the model parameter associated with the relaxation rate in the absence of field inhomogeneities ($\frac{1}{T_{20}}$) [2]. In an ideal condition, where all samples are prepared identically, the value of $\frac{1}{T_{20}}$ should be the same. However, due to the complex procedures, involving manual procedures, involved in sample preparation one might expect some variation of $\frac{1}{T_{20}}$ values across samples. Our results showed that fitting the Jensen-Chandra model to the control cells provided $\frac{1}{T_{20}}$ value of less than 0, which is inappropriate to interpret in a physical sense. We have only applied the theoretical models

without constraining $\frac{1}{T_{20}}$. However, two other studies [16,17] compared the Luz-Meiboom and the Jensen-Chandra models in both constrained as well as non-constrained forms but found contradictory results regarding which form fit the data better. Therefore, it would be interesting to investigate the effect of constraining $\frac{1}{T_{20}}$ based on various assumptions.

In the present work, R_2 dependence on 2τ was observed in MagA+Fe through the expression of a reporter gene, *MagA*, and iron-supplementation. However, this expression is just one type of reporter gene that can be used for this purpose. It would be interesting to investigate the dependence of R_2 on 2τ in other iron-labeled systems such as the over-expression of modified ferritin subunits. This would be a valuable comparison as the MR contrast, from the expression of ferritin, has also been used and compared to that of *MagA* in the past using different MR parameters (signal voids, as well as single R_2, R_2*, and R_2' values) [12,18]. As the exact mechanism of iron handling in MagA-expressing cells is not known, we may speculate on the possibility of the iron storage in MagA-expressing cells to be in a different form than in modified ferritin cells. Model parameters, such as the spatial correlation length (r_c), can potentially provide information on the difference, if any, in spatial distribution of iron in these cells. Furthermore, as relaxation rates are influenced by the form of iron [19,20], R_2 dependence on 2τ may also be dependent on the form of iron storage in these cells. It would be interesting to test the ability of this measurement to distinguish these cells and different forms of iron.

In addition, implementing an MRI acquisition sequence for analyzing the R_2 dependence on 2τ in a small animal model system would be of interest. Technical work would be required to translate the NMR measurement methods of this thesis to a small animal MRI system and to optimize such measurements for accurate R_2 measurements with multiple pulses. It may require optimization using different imaging sequences (i.e., 2D or 3D). Based on the results of this thesis, the most rapid changes in R_2 with respect to 2τ occur in the short 2τ region ($\sim< 2$ ms) in gene-based, iron-labeled cells. Therefore, short RF pulses, strong gradients and possibly magnetization preparation [13, 14] may be required. At first, experiments on phantoms would be beneficial for testing the validity of such measurement on a small animal MRI system. Once the successful translation to small animal MRI is accomplished, analysis of R_2 dependence on 2τ in MagA-expressing cells could be extended to the analysis of tumor xenografts grown from

transplanted cells over-expressing MR reporter genes. Such a xenograft analysis could potentially provide insight into the degree of R_2 dependence on 2τ in engineered animal tissues, which may be different from that observed in a compact pellet of cells. Identifying parameters that influence the relationship between R_2 and 2τ in tissues and organs from animal studies would aid the development of improved MRI methods for pre-clinical animal studies involving cell tracking. Ultimately, *MagA* and other reporter genes will allow us to also assess cellular activity as well as cell location to provide insights regarding disease progression and to monitor cell-based regeneration therapies

3.3 Conclusion

In addressing the objectives of this thesis, the increase in R_2 as a function of 2τ was demonstrated in iron-supplemented, MagA-expressing cells, similar to that previously observed in iron-containing tissues. A similar relationship was also observed in control cells but to a lesser degree (i.e., smaller amplitude and reached a plateau faster). The Jensen-Chandra and the Luz-Meiboom models were applied to R_2 versus 2τ data obtained from iron-supplemented, MagA-expressing cells and their controls. Based on coefficient of non-determination $(1 - r^2)$ analysis, the Jensen-Chandra model provided better fits than the Luz-Meiboom model in this sample. On the contrary, only the Luz-Meiboom model was shown to fit to the control cells.

3.4 References

[1]   Z. Luz, S. Meiboom, Nuclear Magnetic Resonance Study of the Protolysis of Trimethylammonium Ion in Aqueous Solution—Order of the Reaction with Respect to Solvent, J. Chem. Phys. 39 (1963) 366–370. doi:10.1063/1.1734254.

[2]   J.H. Jensen, R. Chandra, NMR Relaxation in Tissues With Weak Magnetic Inhomogeneities., Magn. Reson. Med. 44 (2000) 144–156. http://www.ncbi.nlm.nih.gov/pubmed/10893533.

[3]   K.R. Thulborn, J.C. Waterton, P.M. Matthews, G.K. Radda, Oxygenation dependence of the transverse relaxation time of water protons in whole blood at high field, Biochim. Biophys. Acta. 714 (1982) 265–270.

[4]   J. Vymazal, R. a Brooks, N. Patronas, M. Hajek, J.W. Bulte, G. Di Chiro, Magnetic resonance imaging of brain iron in health and disease., J. Neurol. Sci. 134 Suppl (1995) 19–26. http://www.ncbi.nlm.nih.gov/pubmed/8847541.

[5]   A. Hocq, N. Brouette, S. Saussez, M. Luhmer, P. Gillis, Y. Gossuin, Variable-field relaxometry of iron-containing human tissues: a preliminary study., Contrast Media Mol. Imaging. 4 (2009) 157–64. doi:10.1002/cmmi.275.

[6]   F.Q. Ye, W.R. Wayne Martin, P.S. Allen, Estimation of the iron concentration in excised gray matter by means of proton relaxation measurements., Magn. Reson. Med. 35 (1996) 285–9. http://www.ncbi.nlm.nih.gov/pubmed/8699938.

[7]   B. Stefanovic, J.G. Sled, G.B. Pike, Quantitative T2 in the occipital lobe: the role of the CPMG refocusing rate., J. Magn. Reson. Imaging. 18 (2003) 302–9. doi:10.1002/jmri.10360.

[8]   Y. Rozenman, X. Zou, H. Kantor, Signal loss induced by superparamagnetic iron oxide particles in NMR spin-echo images: the role of diffusion., Magn. Reson. Med. 14 (1990) 31–39. http://www.ncbi.nlm.nih.gov/pubmed/2352471.

[9]   F.Q. Ye, P.S. Allen, Relaxation enhancement of the transverse magnetization of water protons in paramagnetic suspensions of red blood cells., Magn. Reson. Med. 34 (1995) 713–20. http://www.ncbi.nlm.nih.gov/pubmed/8544692.

[10]   J.M. Gomori, R.I. Grossman, H.R. Drott, MR relaxation times and iron content of thalassemic spleens: an in vitro study., AJR. Am. J. Roentgenol. 150 (1988) 567–9. doi:10.2214/ajr.150.3.567.

[11]   R.G. Bryant, K. Marill, C. Blackmore, C. Francis, Magnetic relaxation in blood and blood clots., Magn. Reson. Med. 13 (1990) 133–44. http://www.ncbi.nlm.nih.gov/pubmed/2319929.

[12]   A. Sengupta, K. Quiaoit, R.T. Thompson, F.S. Prato, N. Gelman, D.E. Goldhawk, Biophysical features of MagA expression in mammalian cells: implications for MRI contrast., Front. Microbiol. 5 (2014) 1–9. doi:10.3389/fmicb.2014.00029.

[13]   F.Q. Ye, W.R.W. Martin, P.S. Allen, Estimation of Brain Iron In Vivo by Means of the Interecho Time Dependence of Image Contrast Imaging Sequences for Iron Estimation, Magn. Reson. Med. 36 (1996) 153–158.

[14]   W.R. Martin, F.Q. Ye, P.S. Allen, Increasing striatal iron content associated with normal aging., Mov. Disord. 13 (1998) 281–6. doi:10.1002/mds.870130214.

[15]   A. Sengupta, MRI Relaxation Rates: A Quantitative Approach to Track Tumour Cells Expressing MagA (MSc Thesis), 2014.

[16]   J.J. Chen, G.B. Pike, Human whole blood T2 relaxometry at 3 Tesla., Magn. Reson. Med. 61 (2009) 249–54. doi:10.1002/mrm.21858.

[17]   B. Stefanovic, G.B. Pike, Human whole-blood relaxometry at 1.5 T: Assessment of diffusion and exchange models., Magn. Reson. Med. 52 (2004) 716–23. doi:10.1002/mrm.20218.

[18]   R. Rohani, R. Figueredo, Y. Bureau, J. Koropatnick, P. Foster, R.T. Thompson, et al., Imaging Tumor Growth Non-invasively Using Expression of MagA or Modified Ferritin Subunits to Augment Intracellular Contrast for Repetitive MRI., Mol. Imaging Biol. 16 (2014) 63–73. doi:10.1007/s11307-013-0661-8.

[19]   A. Yilmazt, M. Bucciolinit, G. Longo, F. Franciolinis, Determination of dependence of spin-lattice relaxation rate in serum upon concentration of added iron by magnetic resonance imaging, Clin. Phys. Physiol. Meas. 11 (1990) 343–349.

[20]   K. Keating, R. Knight, A laboratory study to determine the effect of iron oxides on proton NMR measurements, Geophysics. 72 (2007) E27–E32. doi:10.1190/1.2399445.

CURRICULUM VITAE

Casey Yesol LEE

Education

Western University, London, ON, Canada   Sep., 2012 - Present
MSc Candidate in Medical Biophysics
           and Collaborative Graduate Program in Molecular Imaging
Supervisors: Drs. Neil Gelman and Donna Goldhawk
Project: *"Quantitative analysis of relaxation rate dependence on interecho time in MagA-expressing, iron-labeled cells"*

University of Toronto, Toronto, ON, Canada   Sep., 2008 – June, 2012
Hon. B. Sc. *with Distinction*, Specialist in Biological Physics

Publication

Lee CY, Thompson RT, Prato FS, Goldhawk DE and Gelman N. Investigating the Relationship between Transverse Relaxation Rate (R2) and Interecho Time in MR Reporter Gene-based Iron-labeled Cells. *Submitted to Journal of Magnetic Resonance for review (Aug. 20th, 2014).*

Presentations

Lee CY, Thompson RT, Prato FS, Goldhawk DE and Gelman N (2014) Transverse Relaxation Rate (R2) Dependence on Interecho Time (2τ) in Gene-based Iron-Labeled Cancer Cells. International Society for Magnetic Resonance in Medicine (ISMRM). Abstract 1480. Milan, Italy (Poster)

Lee CY, Thompson RT, Prato FS, Goldhawk DE and Gelman N (2014) Investigating Transverse Relaxation Rate (R2) Dependence on Interecho Time (2τ) in Gene-based Iron-labeled Cells. Cell Tracking Symposium. London, Canada (selected for Power poster presentation)

Lee CY, Thompson RT, Prato FS, Goldhawk DE and Gelman N (2014) Investigating Transverse Relaxation Rate (R2) Dependence on Interecho Time (2τ) in MagA-expressing Cells. London Health Research Day. London, Canada (Poster)

Lee CY, Thompson RT, Prato FS, Goldhawk DE and Gelman N (2014) Influence of Change in Interecho time (2τ) on Transverse Relaxation Rate (R2) in MagA-expressing Cells. Imaging Network Ontario (ImNO). Toronto, Canada (Poster)

Lee CY, Thompson RT, Prato FS, Goldhawk DE and Gelman N (2013) Transverse Relaxation Rate (R2) Dependence on Refocusing Pulse Interval (2τ) in MagA-expressing, Breast/Melanoma Tumor Cells. World Molecular Imaging Congress (WMIC). Abstract LBAP 129. Savannah, USA (Poster)

Lee CY, Thompson RT, Prato FS, Goldhawk DE and Gelman N (2013) Transverse Relaxation Rate (R2) Dependence on Interecho Time (2τ) in MagA-expressing Tumor Cells. Imaging Applications in Prostate Cancer Workshop. Abstract 15. London, Canada (Poster)

Lee CY, Thompson RT, Prato FS, Goldhawk DE and Gelman N (2013) Relaxation Rate (R2) Dependence on Refocusing Pulse Interval (2τ) in MagA-expressing, Breast/Melanoma Tumor Cells. London Imaging Discovery. Abstract 30. London, Canada (Poster)

Lee CY, Thompson RT, Prato FS, Goldhawk DE and Gelman N (2013) Measuring relaxation rates of MagA-expressing, breast/melanoma tumor cells at 9.4 Tesla. London Health Research Day. Abstract 41. London, Canada (Poster)

Related Experience

Undergraduate Project Mentor   Sep., 2013 – Apr., 2014
Project: *"Investigating T2* and T1 of mummy bone samples"*

Research Assistant   May, 2011 – Aug., 2011
Supervisor: Dr. Anton Zilman
Department of Physics, University of Toronto
Project: "*Predicting the deterministic and stochastic growth of two bacterial systems using Mathematica*"

Laboratory Assistant (Work-Study)   May, 2011 – Aug., 2011
Department of Physics, University of Toronto

Scholarships and Awards

Western Graduate Research Scholarship   Sep., 2012 – Aug., 2014

University of Toronto Entrance Scholarship   Sep., 2008

Principals' of Woodsworth College Admission Scholarship   Sep., 2008

Governor General's Medal (Bronze)   June, 2008
        With Louis Riel School Division Legacy Scholarship

Memberships

Student member of World Molecular Imaging Society (WMIS)   2013
Student member of International Society for Magnetic Resonance in Medicine (ISMRM)
                                                                            2014

Extra-Curricular and Volunteer Activities

Assistant organizer   Sep., 2013 – Apr., 2014
        Lawson Research Institute's "Talks on Fridays"
        -Assisted with organization and introduction of speakers for weekly seminar series

Let's Talk Science   Sep., 2013 – Current
        -A student organization that promotes science to local youth

Volunteered as a Korean-English interpreter/tutor   2013